https://doi.org/10.5194/egusphere-2025-3910
Preprint. Discussion started: 9 September 2025

A Microwave Scattering Database of Oriented Ice and Snow Particles: Supporting Habit-Dependent Growth Models and Radar Applications (McRadar 1.0.0)

Leonie von Terzi[1], Davide Ori[2], and Stefan Kneifel[1]

[1]Institute of Meteorology, Ludwig-Maximilians University, Munich, Germany
[2]Institute of Geophysics and Meteorology, University of Cologne, Cologne, Germany

Correspondence: Leonie von Terzi (l.terzi@lmu.de)

Abstract.

The optical properties of atmospheric hydrometeors are a crucial component of any forward operator. These forward operators are essential data assimilation, and atmospheric model evaluations. Recent advances in microphysical modelling, such as Lagrangian super-particle models with habit prediction for ice particles, allow for the continuous evolution of particle properties in contrast to fixed hydrometer classes with fixed properties. This increasing complexity demands scattering databases capable of handling a wide range of particle properties.

The discrete dipole approximation (DDA) is one of the most accurate and widely used methods for computing the scattering properties of irregular ice particles. However, its high computational cost typically limits either the diversity of particle shapes or the range of environmental parameters (e.g., frequency, temperature) represented in existing databases, constraining their applicability to models with highly variable microphysics.

In this study, we present a new DDA-based database of optical properties at 5.6, 9.6, 35.6, and 94 GHz, specifically designed to accommodate the broad range of ice crystal morphologies predicted by habit-evolving schemes. The database contains 2,627 individual ice crystals, including dendrites, plates, and columns, as well as 450 aggregates with varying degrees of riming and crystal types. The data are organized in three levels: Level 0 provides raw scattering matrices at individual orientations for a full range of scattering angles; level 1a summarizes Mueller and amplitude matrix elements relevant for radar applications (at forward and backward scattering angles); and level 1b offers lookup tables of scattering properties that are relevant for polarimetric radars assuming azimuthally random orientations of the particles. These data allow for flexible treatment of the canting angle of the particles. The lookup tables are directly accessible via the McRadar simulator and can also be interfaced with other forward operators.

The new database allows for a more consistent and realistic treatment of evolving ice particle properties in atmospheric models, improving the interpretation of radar observations and model-observation integration.

https://doi.org/10.5194/egusphere-2025-3910
Preprint. Discussion started: 9 September 2025

1 Introduction

The ice phase in clouds plays a crucial role in numerical weather prediction and climate modelling, as approximately 75% of precipitation reaching the ground forms via ice-phase processes (Heymsfield et al., 2018). However, significant knowledge gaps remain regarding ice microphysical processes, leading to substantial uncertainties in their parametrizations within models (Morrison et al., 2020). Forward models operating in the microwave region are essential for the development of retrieval techniques, both for active and passive microwave observations, and for the assimilation of satellite data into models (Geer et al., 2018). A key component of such forward models is the availability of comprehensive databases of particle optical properties (Maahn et al., 2020).

Estimating the optical properties of ice particles is a challenging task. In the microwave region, accurately characterizing these properties requires detailed knowledge of the particles' microphysical characteristics, including size, mass, density, shape, internal structure, and composition. The complex structures of ice particles can be modelled using physical snow growth models that simulate depositional growth, aggregation, and riming, such as the aggregation model introduced by Leinonen and Moisseev (2015) and later extended by Karrer et al. (2020). Once the particle shape is determined, its optical properties must be computed using numerical methods. A widely used technique for calculating the polarimetric radar signatures of ice particles is the T-matrix method, which approximates ice particles as spheroids with a homogeneous mass distribution (Mishchenko et al., 1996). This allows for a flexible treatment of mass, size, aspect ratio and density, which is convenient when trying to represent various shapes of (ice) particles. However, real snowflakes typically exhibit highly inhomogeneous internal mass distributions that strongly influence their scattering characteristics (Sorensen, 2001). As a result, T-matrix methods often underestimate polarimetric signals for complex particles such as aggregates (e.g., Petty and Huang, 2010; Schrom and Kumjian, 2018; Kneifel et al., 2020).

The Discrete Dipole Approximation (DDA) (Draine and Flatau, 1994) has become one of the most widely used and accurate methods for calculating the scattering properties of irregularly shaped particles. DDA discretizes the particle onto a grid of dipoles and can accommodate arbitrary shapes. It has been extensively validated (Yurkin and Hoekstra, 2007), but its high computational cost, scaling approximately with $O(nlogn)$, where n is the number of dipoles, remains a significant limitation. During the last decade, increased computational power has facilitated the development of DDA databases. Many of these databases (Liu, 2008; Kuo et al., 2016) assume randomly oriented ice particles, which limits their applicability to polarimetric radar observations. More recent efforts, such as Lu et al. (2016) and Brath et al. (2020), have provided scattering properties across a range of orientations. For example, the Lu et al. (2016) database includes over 1,000 ice particles, ranging from single crystals to aggregates and graupel, at X-, Ku-, Ka-, and W-band frequencies. While this database offers broad shape representation, Brath et al. (2020) focused on a smaller number of particles but extended the frequency range, supporting applications up to the sub-mm region.

Advances in microphysical modelling have introduced habit prediction schemes that simulate the morphological evolution of ice crystals during depositional growth (Welss et al., 2024; Jensen et al., 2017; Jensen and Harrington, 2015; Harrington et al., 2013). The shape of ice crystals influences the particles fall velocity, the growth through deposition, riming and aggregation as

https://doi.org/10.5194/egusphere-2025-3910
Preprint. Discussion started: 9 September 2025

well as their radiative properties. Especially for polarimetric radar observations, predicting the shape of ice crystals is crucial (Schrom and Kumjian, 2019). In contrast to traditional ice-particle models, where crystals are represented by a single, predefined type (e.g., a dendrite) with fixed mass-size and aspect-ratio-size relationships, habit-prediction schemes evolve particle mass, size, density, and aspect ratio continuously in response to ambient temperature and supersaturation (Welss et al., 2024). Recently, new bulk microphysical schemes have emerged that eliminate predefined ice classes altogether. Instead, they employ one or more particle categories in which the physical properties are predicted directly from environmental conditions, such as in the Predicted Particle Properties (P3) scheme (Morrison et al., 2025). Both the P3 model and habit-prediction approaches require a consistent, continuous treatment of ice-particle properties in scattering databases. While spheroidal methods such as the T-matrix offer flexibility by allowing particle properties to vary continuously, they can introduce substantial errors in forward simulations, especially for dendritic crystals and polarimetric radar variables (Schrom and Kumjian, 2018). Microwave scattering properties of realistically shaped ice crystals are needed in order to accurately forward simulate the complex model output. For accurate forward simulations, microwave scattering properties based on realistically shaped ice crystals are therefore essential. However, because habit-prediction schemes represent particles as spheroids, the internal mass distribution remains uncertain, creating a major source of error when selecting representative shapes for forward simulations.

This uncertainty was investigated by Schrom and Kumjian (2019). They developed a probabilistic forward operator that maps microphysical model output to radar observations using both DDA-derived scattering properties and equivalent spheroidal approximations. Their method involved statistically fitting equivalent spheroids to match the backscatter cross-section at horizontal polarization (σ_h) and ZDR of complex crystals. This mapping enabled the quantification of uncertainties arising from dendritic branching; for example, a standard deviation of ± 0.5 dB in ZDR at X-band was reported.

Even greater uncertainties are expected for snow aggregates, which consist of multiple ice crystals with varied shapes and orientations. Ori et al. (2021) demonstrated the potential bias introduced when using a single representative aggregate for a given size or mass by comparing single-particle DDA results to ensemble averages.

Both Schrom and Kumjian (2019) and Ori et al. (2021) emphasize the need for a scattering database that supports forward simulation of complex microphysical model output, while minimizing errors associated with spheroidal approximations or limited particle shape diversity. In this study, we present a new DDA-based scattering database that addresses this need. The database includes the scattering properties of 3,077 ice particles at C- (5.6 GHz), X- (9.6 GHz), Ka- (35.6 GHz), and W-band (94 GHz) frequencies. Scattering properties are provided for elevation angles from -90° to 90° in 5° steps and azimuth angles from 0° to 360° in 22.5° steps. The database includes 2,627 ice crystals, encompassing dendrites, plates, and needles, as well as 450 aggregates with varying crystal types and degrees of riming.

The forward and backward scattering properties at all elevations and azimuth directions of all particles are freely available. Additionally, we provide averages of azimuthally random orientations for each particle to enable flexible canting-angle assumptions in forward operators[1]. In this study, we also introduce a forward operator (Section 4.1) that maps microphysical particle properties into radar observables. Unlike Schrom and Kumjian (2019), our approach uses ensemble-averaged scatter-

[1] see https://doi.org/10.5281/zenodo.16792943

https://doi.org/10.5194/egusphere-2025-3910
Preprint. Discussion started: 9 September 2025

ing properties, derived by averaging over a number of nearest neighbours in microphysical property space. Finally, we present two application examples that illustrate the strengths of this new database.

2 Ice Particle Properties

The habit of ice crystals varies depending on the ambient temperature and supersaturation (Libbrecht, 2017). Recent advancements in bin and Lagrangian particle microphysical models, including those with habit prediction capabilities, have created a demand for scattering databases that allow consistent forward simulation of model output. To meet this need, we have developed a comprehensive scattering database containing 3,077 ice particles, including 2,627 ice crystals and 450 aggregates. All particles were generated using the aggregation model described by Leinonen and Moisseev (2015). While the aggregate shapes were taken from previous studies (Ori et al., 2021; Karrer et al., 2020), the ice crystal shapes were specifically created for this database.

2.1 Ice Crystals

In the dendritic growth layer (corresponding to temperatures between $-20°$C and $-10°$C), supersaturation levels significantly influence the degree of branching in plate-like crystals, resulting in a wide variety of morphologies (Bailey and Hallett, 2004, 2009; Lohmann et al., 2016; Takahashi, 2014; Libbrecht, 2017). Takahashi (2014) categorized these forms as sector, broad-branch, stellar, dendritic, and fern-like structures. This high degree of complexity of the internal structure of dendritic ice crystals cannot be explicitly described in habit prediction schemes such as the one implemented in Welss et al. (2024). The habit prediction schemes therefore describe ice crystals as porous spheroids, whose aspect ratio and density is varied by the habit prediction. A detailed description is given in 5.1. While the description of ice crystals as spheroids gives reasonably well results when comparing the aspect ratio, mass and maximum dimension (D_{max}) to laboratory studies (Welss et al., 2024), it is well known that the internal structure of ice particles is essential for scattering in the microwave regime (e.g. Kneifel et al., 2020; Ori et al., 2021; Brath et al., 2020). In order to forward simulate the output of models using habit prediction schemes, a large variety of ice crystal shapes has to be used, in order to match the predicted aspect ratios, densities, masses, and D_{max}.

To capture the morphological diversity of dendritic ice crystals, we therefore employed the Reiter-algorithm (Reiter, 2005) as implemented by Leinonen and Moisseev (2015). By varying three key parameters,α, β, and γ, the shape of the dendrite can be varied. As the generation of dendrites is time intensive, (Leinonen and Moisseev, 2015) has generated one default dendrite, which is then used in the aggregation process. This dendrite follows the aspect-ratio size relationship described in Leinonen and Moisseev (2015); Pruppacher and Klett (1997). This single dendritic shape is not enough to cover the rich output of the habit prediction, where a large variety of aspect ratios, densities, masses, and sizes are possible, depending on the individual particle growth history. Therefore, we used the Reiter algorithm to generate a large variety of dendritic shapes. Specifically, we set $\alpha = 1$ and varied β between 0.2 and 0.7 and γ between 0.0001 and 0.006. D_{max} ranged from 10 μm to 7 mm. Figure 1 presents a subset of the resulting ice crystal shapes.

https://doi.org/10.5194/egusphere-2025-3910
Preprint. Discussion started: 9 September 2025

The variety in aspect ratios generated by the Reiter algorithm alone is not enough to cover the entire aspect ratio space predicted by the habit prediction. In extreme cases, a particle can change growth regime from e.g., the columnar growth regime assumed at temperatures colder than -22° C into the plate-like growth regime at temperatures between -20 and -10° C. Bailey and Hallett (2004) have shown that when such a regime change happens, the particle is likely to decrease its aspect ratio towards unity, effectively generating a "thick" column. To capture these particles, we adapted the aggregation model from Leinonen and Moisseev (2015) to allow the generation of ice crystals with adjustable aspect ratios at fixed $D_{\max}$. This was done by effectively stacking dendritic particles of the same shape on top of each other, increasing the aspect ratio towards unity. In total, we generated 1,850 dendritic ice crystals.

At smaller sizes or under low supersaturation conditions, solid plates are more likely to form. To represent this regime, we generated 625 plate-like crystals with varying sizes, masses, and aspect ratios with Leinonen and Moisseev (2015) and our adaptation to allow more flexible aspect ratios. In the temperature range between -10°C and -5°C, ice crystals tend to grow into columnar shapes (Bailey and Hallett, 2009). Accordingly, we used the aggregation model to generate 125 columnar crystals, again varying size, mass, and aspect ratio.

The resulting mass–size and aspect ratio–size relationships for all 2,600 ice crystals are illustrated in Figure 2.

2.2 Aggregates

Similarly to ice crystals, the microphysical properties of aggregates vary largely depending on the ice crystals which generated the aggregate and stochastic parameters determined during the collision process, such as the angle between the colliding partners, or the contact point (e.g. Locatelli and Hobbs, 1974; Mitchell et al., 1996; Westbrook et al., 2004). Therefore, we have randomly selected 450 aggregates of plates, dendrites, mixtures of dendrites and columns (mix2) with a riming equivalent liquid water content (see Leinonen and Moisseev (2015)) between 0 and 1kg m^{-2} from the snow library of snowScatt (Ori et al., 2021). The resulting database comprises 175 rimed particles, 106 mixtures of columns and dendrites, 105 dendrite aggregates, and 63 plate aggregates. The microphysical properties of all aggregates are shown in Fig. 4.

3 Radar scattering properties

3.1 Reference frames

We first define two fundamental reference frames, namely the radar reference frame (RRF), and the particle reference frame (PRF). The RRF (often called laboratory reference frame) can be considered as the most general one, it is solid with a hypothetical ground-based radar, the z-axis goes along the vertical with respect to the radar location, while the orientation of the horizontal xy-axes is arbitrary. The radar reference frame defines the coordinates of the propagation direction of the radar beam and its polarization planes (Fig. 5a). The propagation direction is defined by the radar elevation angle el and azimuth az. The vertical polarization plane spans the beam propagation direction and the z-axis, while the horizontal polarization plane is orthogonal to the vertical and also contains the beam propagation vector.

https://doi.org/10.5194/egusphere-2025-3910
Preprint. Discussion started: 9 September 2025

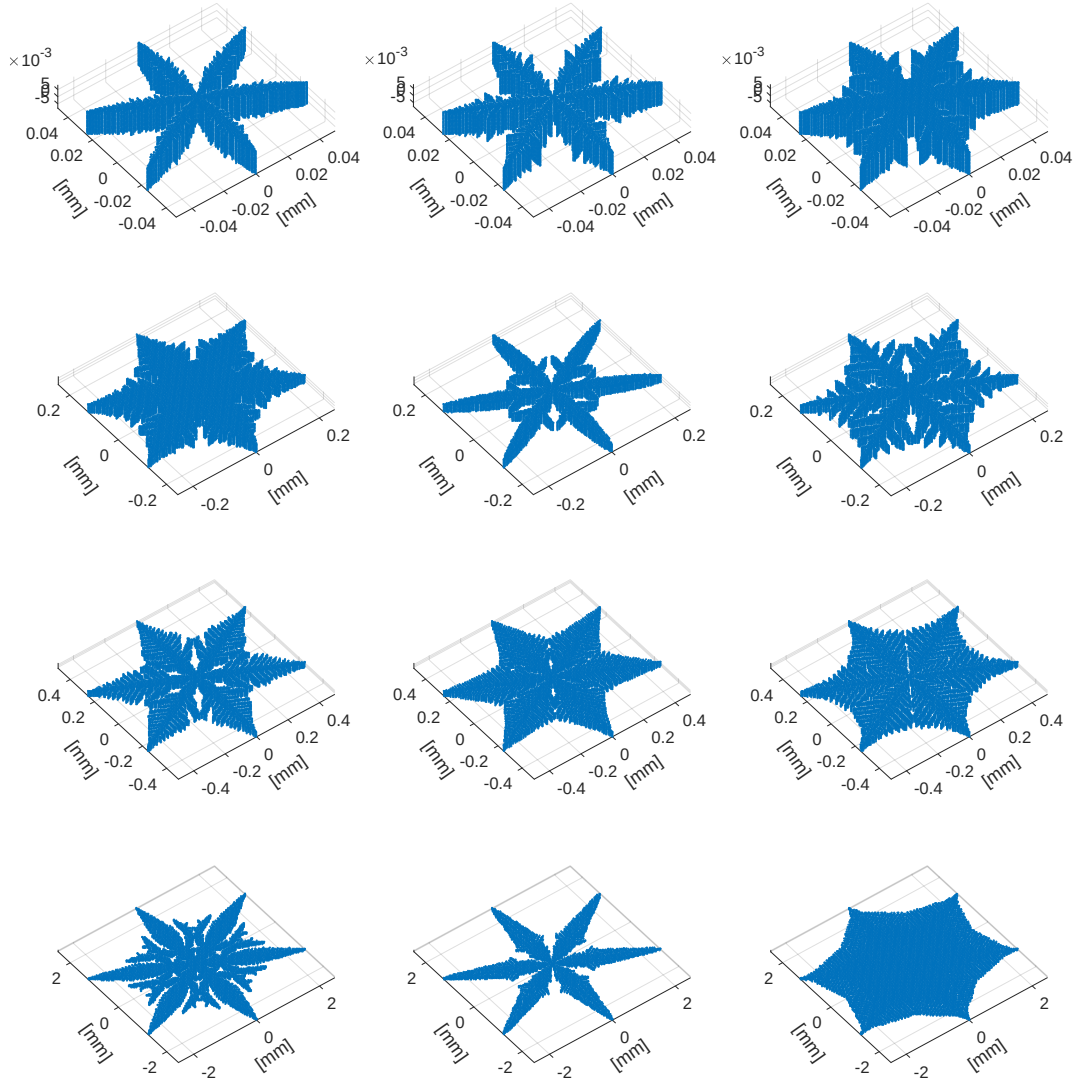

Figure 1. Examples of dendritic ice crystal shapes from the scattering database. The first row shows dendrites with a D_{max} of 100 μm, the second row with 500 μm, the third row with 1 mm and the last row with 5 mm.

https://doi.org/10.5194/egusphere-2025-3910
Preprint. Discussion started: 9 September 2025

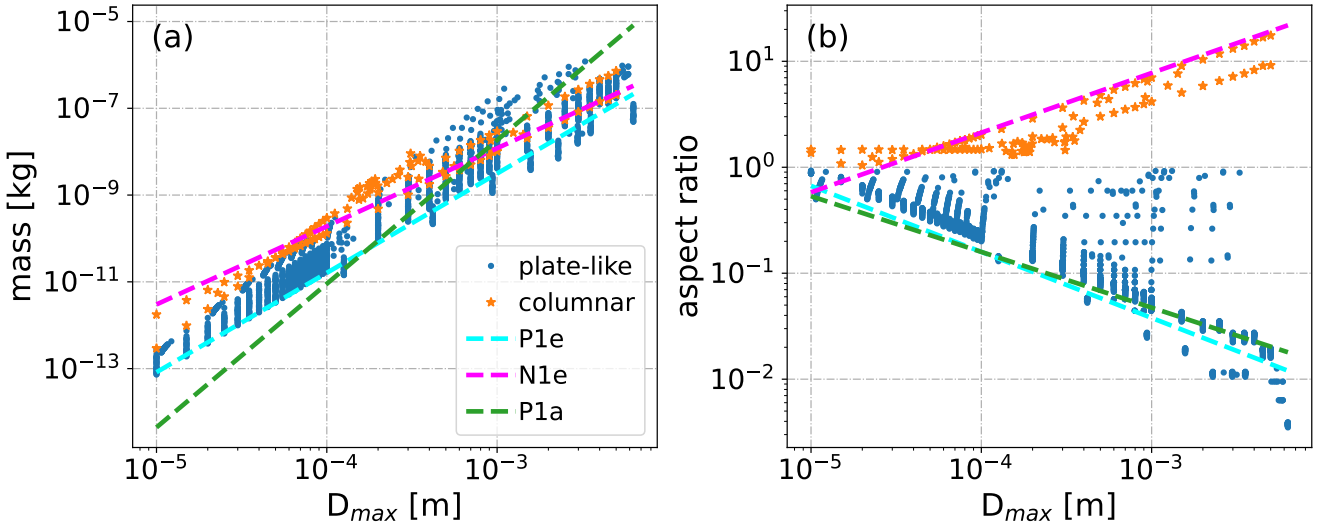

Figure 2. Ice particle mass (a) and aspect ratio (b) as a function of the maximum dimension (D_{max}). Orange asterisks denote columnar, blue dots denote plate-like particles. For comparison, the relationships of the Pruppacher and Klett (1997), plate (P1a), dendrite (P1e) and needle (N1e) are shown.

The PRF is solid with the snow particle, and is assumed to correspond to the particle axes of inertia with the shortest inertia axis aligned with the z-axis of the PRF. The transformation from the PRF to the RRF is performed by means of 3 Euler rotations (angles α, β, and γ) that follow the commonly used zyz-convention (Fig. 5b). With respect to the PRF, the propagation direction of any vector is defined by the polar coordinates θ and ϕ.

The polarimetric scattering properties of a complex-shaped snowflake in the RRF would in general depend on all 5 angles (el, az, α, β, γ). Note that a rotation of the angle az corresponds to an inverse rotation of the angle α, which implies that the dependence on the angle az can be dropped without loss of information.

3.2 Single-scattering particle properties

At a given particle orientation, the incident electromagnetic field E^i can be related to the scattered (far-) field E^s via the amplitude scattering matrix:

$$\begin{bmatrix} E^s_{\parallel} \\ E^s_{\perp} \end{bmatrix} = \frac{\exp(ikr)}{-ikr} \begin{bmatrix} S_1 & S_4 \\ S_3 & S_2 \end{bmatrix} \begin{bmatrix} E^i_{\parallel} \\ E^i_{\perp} \end{bmatrix} \tag{1}$$

the subscripts $\parallel$ and $\perp$ indicate parallel and perpendicular orientations with respect to the scattering plane, $i = \sqrt{-1}$, $k = 2\pi/\lambda$ is the wavenumber, r is the distance between the scatterer and the observation point, and $S_{1,\ldots,4}$ are the complex elements of the amplitude matrix. The amplitude matrix can be converted to the Mueller matrix Z, which relates the Stokes vector of the

https://doi.org/10.5194/egusphere-2025-3910
Preprint. Discussion started: 9 September 2025

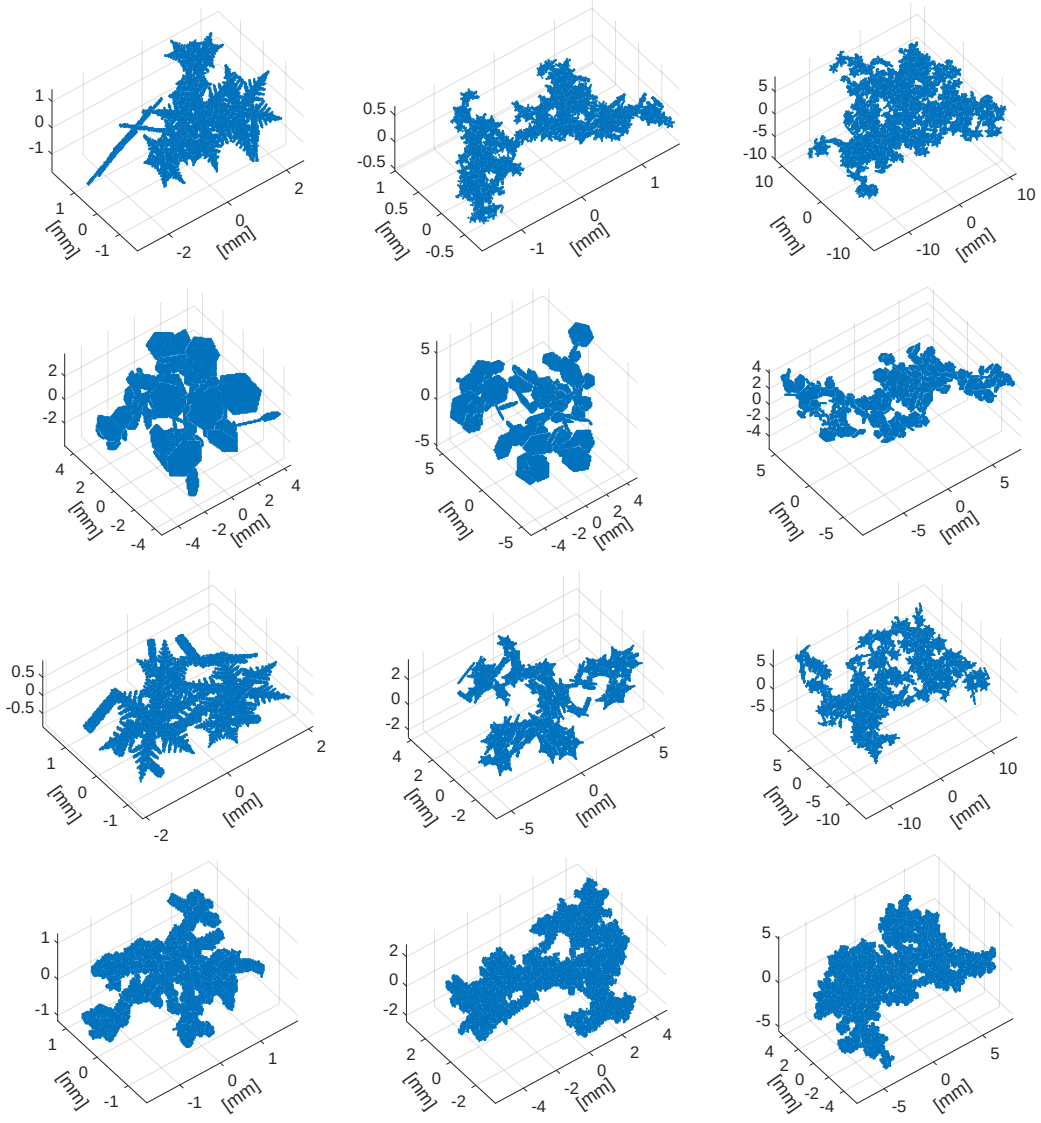

Figure 3. Examples of aggregates available in the scattering database. Shown are dendrite aggregates (top row), plate aggregates (second row), aggregates consisting of a mixtures of dendrites and columns (mix2) (third row) and rimed mix2 aggregates (fourth row).

https://doi.org/10.5194/egusphere-2025-3910
Preprint. Discussion started: 9 September 2025

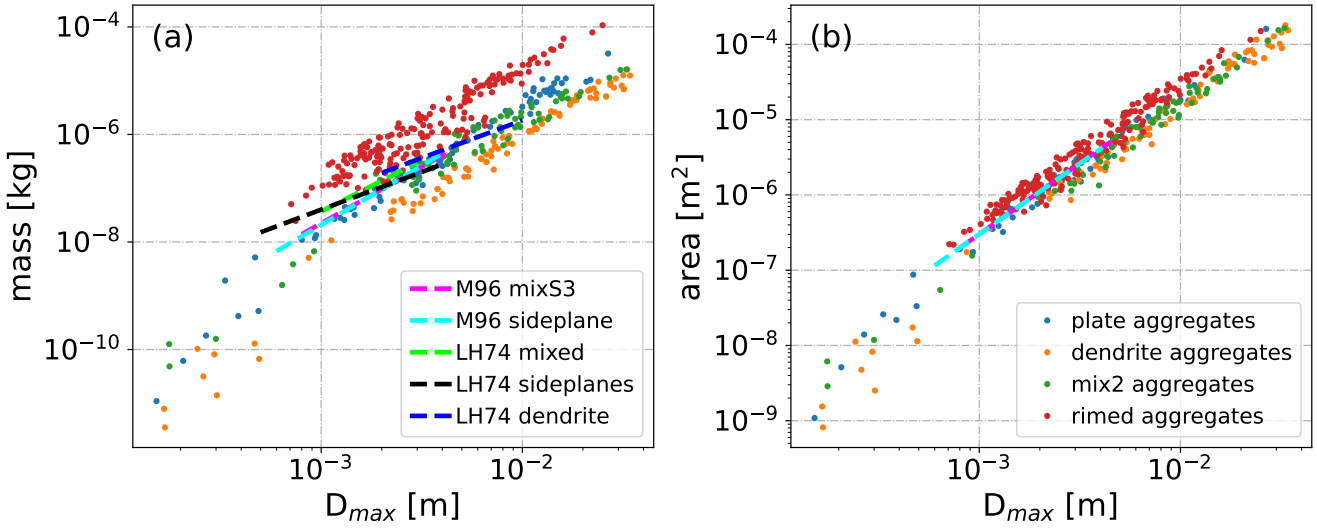

Figure 4. Aggregate mass (a) and cross-sectional area (b) as function of D_{max}. For comparison, the relationships of Mitchell (1996) for aggregates of side planes (M96 sideplane), aggregates of side planes, columns and bullets (M96 mixS3) as well as the relationships of Locatelli and Hobbs (1974) for aggregates of unrimed radiating assemblages of dendrites (LH74 dendrite), aggregates of unrimed radiating assemblages of plates, side planes, bullets and columns (LH74 mixed) and aggregates of unrimed side planes (LH74 sideplanes) are shown. Note: area-size relationships are only available for the Mitchell et al. (1996) aggregates.

incoming and scattered fields:

$$\begin{bmatrix} I_{sca} \\ Q_{sca} \\ U_{sca} \\ V_{sca} \end{bmatrix} = \frac{\exp(-2r\mathrm{Im}(m)k_{\mathrm{sca}})}{|k_{\mathrm{sca}}^2|\,r^2} \begin{bmatrix} Z_{11} & Z_{12} & Z_{13} & Z_{14} \\ Z_{21} & Z_{22} & Z_{23} & Z_{24} \\ Z_{31} & Z_{32} & Z_{33} & Z_{34} \\ Z_{41} & Z_{42} & Z_{43} & Z_{44} \end{bmatrix} \begin{bmatrix} I_{in} \\ Q_{in} \\ U_{in} \\ V_{in} \end{bmatrix} \tag{2}$$

where $\mathrm{Im}(m)$ is the imaginary part of the refractive index m and $Z_{11,\ldots,44}$ are the complex elements of the Mueller matrix. In contrast to the Amplitude matrix, the Mueller matrix contains only information about the intensity of the scattered wave, not the absolute phase. The Amplitude matrix can be converted into the Mueller matrix following well established formulas. For further discussion of the Mueller and Amplitude matrix, the reader is referred to the User Manual of the ADDA code (Yurkin and Hoekstra, 2011). Both matrices were calculated with the amsterdam discrete dipole approximation (ADDA) code (Yurkin and Hoekstra, 2011) and are available in the scattering database at C- (5.6GHz), X- (9.6GHz), Ka- (35.6GHz) and W- (94.0GHz) Band as well as for el between 0° and 180° in 5° steps and az between 0° to 337.5° in 22.5° steps for every scattering direction. The scattering properties were calculated at a temperature of 270K, using the refractive index model described in Mätzler (2006), Chapter 5 for ice.

https://doi.org/10.5194/egusphere-2025-3910
Preprint. Discussion started: 9 September 2025

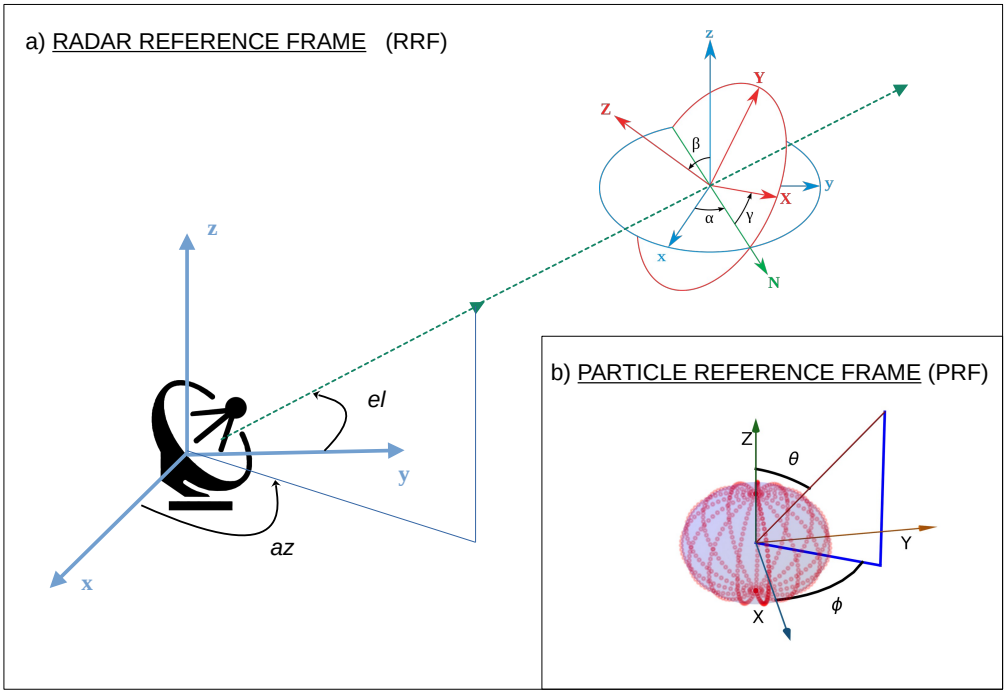

Figure 5. Panel a, Schematic representation of the Radar Reference Frame (RRF in blue) and the rotation of the Particle Reference Frame (PRF in red) with respect to the RRF employing the three Euler angles (α, β and γ). Panel b, Detail of the unrotated PRF and the polar coordinates (θ,ϕ) that define any unit vector in the PRF. The red dots represent the set of sampling directions used in section 3.4 to describe the particle scattering in all possible orientations.

After converting the amplitude matrix into forward scattering alignment (FSA) convention by multiplying the entries with $\frac{i}{k}$, typical radar parameters can be calculated as follows:

– Radar reflectivity factor at horizontal polarization

$$Ze_{\mathrm{hh}} = \frac{2\lambda^4}{\pi^4 |K|^2} \left(Z_{11}|_{180^\circ} + Z_{22}|_{180^\circ} + Z_{12}|_{180^\circ} + Z_{21}|_{180^\circ} \right) \tag{3}$$

– Radar reflectivity factor at vertical polarization

$$Ze_{\mathrm{vv}} = \frac{2\lambda^4}{\pi^4 |K|^2} \left(Z_{11}|_{180^\circ} + Z_{22}|_{180^\circ} - Z_{12}|_{180^\circ} - Z_{21}|_{180^\circ} \right) \tag{4}$$

– Extinction cross-section at horizontal and vertical polarization:

$$c_{\mathrm{ext,hh}} = \frac{4\pi \mathrm{Im}\left(S_2|_{0^\circ}\right)}{k}; \quad c_{\mathrm{ext,vv}} = \frac{4\pi \mathrm{Im}\left(S_1|_{0^\circ}\right)}{k} \tag{5}$$

https://doi.org/10.5194/egusphere-2025-3910
Preprint. Discussion started: 9 September 2025

– Specific differential phase shift:

$$\mathrm{KDP} = \frac{180\lambda\left(\mathrm{Re}(S_2|_{0^\circ}) - \mathrm{Re}(S_1|_{0^\circ})\right)}{\pi} \tag{6}$$

where λ is the wavelength, $|K|^2$ the dielectric factor and $\mathrm{Im}(var), \mathrm{Re}(var)$ the imaginary and real parts of the variable var respectively and the subscript $0^\circ, 180^\circ$ refers to the scattering direction, with 0° being forward and 180° backward.

3.3 Orientation averaging

Radar polarimetric quantities are sensitive to the shape and orientation of the particles. The steady-state falling orientation of a complex-shaped particle, such as a snowflake, is determined by the complex equilibrium of gravitational and aerodynamic forces. The problem of finding the fall attitude of a snowflake is further complicated by the fact that such a stationary orientation might not even exist (i.e., snowflakes can continuously tumble and spin (McCorquodale and Westbrook, 2021)), furthermore, hydrometeors typically fall in an environment that is itself non-stationary and turbulent. For this study, we assumed that snowflakes fall by default by aligning their longest axis of inertia horizontally.

The attitude of a snowflake during its fall can be described by the probability distribution ($f_\alpha(\alpha)$, $f_\beta(\beta)$, $f_\gamma(\gamma)$) of the three Euler angles that define its orientation with respect to the default fall configuration. The average value of a quantity $\mathbf{S}(\alpha,\beta,\gamma)$ that depends on the orientation of the particle can be calculated as Brath et al. (2020)

$$\langle \mathbf{S} \rangle_{\alpha,\beta,\gamma} = \int_0^{2\pi}\int_0^{\pi}\int_0^{2\pi} \mathbf{S}(\alpha,\beta,\gamma) f_\alpha(\alpha) f_\beta(\beta) \sin(\beta) f_\gamma(\gamma) \mathrm{d}\alpha \mathrm{d}\beta \mathrm{d}\gamma \tag{7}$$

Since a radar observes the hydrometeor population over a certain amount of time, during which particles change their orientation through i.e. tumbling and spinning movements, we are not interested in the scattering properties of a single oriented particle. Rather, we are interested in the scattering properties of a particle which has different orientations, which can be represented as multiple particles differently oriented but otherwise identical. It is widely accepted that the α and γ angles follow a uniform distribution (Mishchenko and Yurkin, 2017). Averaging over the distributions of α and γ leads to the representation of polarimetric scattering properties that follow the so-called *azimuthally random orientation* (ARO) assumption (Brath et al., 2020). Under these conditions, the polarimetric scattering properties of snowflakes depend on only two angles, namely the radar elevation angle el and the particle canting angle β.

$$S_{\mathrm{ARO}}(el,\beta) = \int_0^{2\pi}\int_0^{2\pi} \frac{S^{\mathrm{RRF}}(el,\alpha,\beta,\gamma)}{4\pi^2} \mathrm{d}\alpha \mathrm{d}\gamma \tag{8}$$

3.4 Sampling discrete scattering orientations

In the previous section, we explained how it is possible to leverage the assumption that hydrometeors have no preferential orientation in the azimuth to reduce the dimensionality of the polarimetric scattering data structure. However, to compute Eq. 8

https://doi.org/10.5194/egusphere-2025-3910
Preprint. Discussion started: 9 September 2025

one would still need to perform a sufficient number of scattering calculations at individual sets of elevation angles and particle orientations $(el, \alpha, \beta, \gamma)$. This is a considerable computational effort, thus, following previous studies (Brath et al., 2020; Lu et al., 2016) we reduce the dimensionality of the problem by realizing that any scattering problem in the RRF (identified by the five angles el, az, α, β, γ) can be represented by a corresponding scattering in the PRF, provided that one can operate a proper transformation between the two reference frames. In the PRF any scattering problem is identified simply by the two polar coordinates (θ_0, ϕ_0) that define the propagation direction of the incoming electromagnetic wave in the PRF. Mathematically $(el, az, \alpha, \beta, \gamma) \Rightarrow (\theta_0, \phi_0)$.

The transformation matrices ρ and ρ^{-1} that allow to convert amplitude matrices from the PRF to the RRF are provided by Mishchenko (2000) and depend on the polar coordinates of the direction of the incoming and scattered beams as well as the three Euler angles defining the orientation of the scatterer. Here, we drop the dependency on the scattered directions for the sake of simplicity, since, for radar applications, the only two relevant scattering directions are the forward and backward ones. Mathematically, one can write

$$\mathbf{S}^{\mathrm{RRF}}(el, az, \alpha, \beta, \gamma) = \rho^{T}(el, az, \alpha, \beta, \gamma)\mathbf{S}^{\mathrm{PRF}}(\theta_0, \phi_0)\rho(el, az, \alpha, \beta, \gamma) \tag{9}$$

Thus, we perform individual scattering calculations in the PRF with a regular (θ_0, ϕ_0) grid. The polar angle θ_0 goes from -90° to 90° with increments of 5° while the azimuth angle ϕ_0 goes from 0 to 360° with increments of 22.5°. The set of directions used is represented as red dots in Fig. 5b. This approach is less efficient than other strategies to sample points over a unitary sphere (such as the icosahedral sampling strategy of Brath et al. (2020)), because it would allow for an increased density of sampling points close to the poles. However, it is fundamentally simple and has the advantage of integrating perfectly over azimuths in the case of non-tumbling ($\beta = 0$) particles.

The azimuth averaging of Eq. 8 is then performed numerically by sampling the database of individual scattering directions using a nearest-neighbour approach, hence $(el, az, \alpha, \beta, \gamma) \Rightarrow (\theta_0^{NN}, \phi_0^{NN})$. The transformation of Eq. 9 is then applied to the sampled matrix before executing the quadrature rule which is equivalent to perform the following integral

$$\mathbf{S}_{\mathrm{ARO}}(el, \beta) = \int_0^{2\pi}\int_0^{2\pi} \frac{\rho^{T}(el, az, \alpha, \beta, \gamma)\mathbf{S}^{\mathrm{PRF}}(\theta_0^{\mathrm{NN}}, \phi_0^{\mathrm{NN}})\rho(el, az, \alpha, \beta, \gamma)}{4\pi^2}\mathrm{d}\alpha\mathrm{d}\gamma \tag{10}$$

3.5 Radar variables derived from the database

At an elevation angle of 30° and β=0°, Ze, ZDR, and KDP at 9.6 GHz (X-band), 35.6 GHz (Ka-band), and 94 GHz (W-band) for all particles in the database are shown in Fig. 6. A notable feature is that small ice crystals in the database can exhibit negative ZDR values, which is counter-intuitive since the particles are horizontally aligned with their largest dimension. For particles with an aspect ratio different from unity, one would generally expect a positive ZDR.

The particles showing negative ZDR are dendritic crystals with aspect ratios close to unity (0.7-0.9). Based solely on aspect ratio, their ZDR should be positive. However, the internal mass distribution is asymmetric: the vertical dimension has a higher mass density than the horizontal dimension (see examples in Fig. 1). When the aspect ratio is near unity, this density difference becomes significant, resulting in a higher vertical Ze and thus a negative ZDR. This effect is not observed for solid plates with

https://doi.org/10.5194/egusphere-2025-3910
Preprint. Discussion started: 9 September 2025

similar size and aspect ratio because their mass distribution is nearly uniform along the vertical and horizontal axes, making aspect ratio the dominant factor for ZDR.

Comparing Ze, ZDR, and KDP at W-Band of the ice crystals in this database with those in Lu et al. (2016) (see their Fig. 4 and Fig. C1 in von Terzi et al. (2022)), we find similar features. Ice crystals with masses exceeding 10^{-8} kg, corresponding to a maximum dimension of approximately 3 mm (see Fig. A1), enter the non-Rayleigh scattering regime, producing a ZDR peak of 12 dB and a flattening of Ze. This behaviour is consistent with Lu et al. (2016), where dendritic crystals reach a maximum W-band ZDR of 9 dB at D_{max}=3 mm. Likewise, KDP in our database aligns with Lu et al. (2016), reaching 0.2 $mm^{\circ}\ km{-}1$ at D_{max}=8 mm when normalized by wavelength (Fig.A1).

Aggregates in our database show some differences from those in Lu et al. (2016). At X-band, aggregates reach a maximum Ze of 27 dBz at a mass of 10^{-4} kg (corresponding to D_{max}≈3.5 cm), whereas in Lu et al. (2016), the maximum Ze for D_{max}≈3 cm is only 9.5 dBz. This higher reflectivity in our dataset is primarily due to rimed aggregates. Unrimed aggregates in our database reach only 5 dBz at D_{max}≈3.5 cm, comparable to Lu et al. (2016).

The transition of aggregates into the Mie-regime occurs at slightly higher masses in our dataset: around 5×10^{-8} kg at W-band, with a pronounced flattening at 5×10^{-7} kg (D_{max}≈2–3 mm). In contrast, Lu et al. (2016) reports the transition at 5×10^{-9} kg. As noted in Lu et al. (2016), their aggregates enter the non-Rayleigh scattering regime earlier than those in Leinonen and Moisseev (2015), likely due to structural differences. Our aggregates consist primarily of plates, dendrites, or a mixture of dendrites and columns, whereas the Lu et al. (2016) aggregates are more akin to aggregates of needles.

ZDR values of aggregates are similar between the two databases: at W-band, most aggregates exhibit ZDR between 2–3 dB. Only high-density rimed aggregates in our dataset reach up to 5.5 dB. KDP also remains in a comparable range to Lu et al. (2016).

4 Database Setup

The scattering database is organized into three hierarchical levels, each corresponding to a different stage of post-processing. Due to the large size, the level 0 data is available upon request.

Level 0 contains the raw output from the ADDA code, including the full amplitude and Mueller matrices for each particle, along with log files documenting the ADDA simulation settings and diagnostics.

In **Level 1a** these outputs are processed by summarizing the amplitude and Mueller matrix entries into `NetCDF` files for each particle type across all elevation and azimuth angles and frequencies.

level 1b further condenses the data into two lookup tables (LUTs), one for monomers and one for aggregates. These LUTs represent the azimuthally random orientational averages of all particles and serve as the input for the radar forward simulator, McRadar.

https://doi.org/10.5194/egusphere-2025-3910
Preprint. Discussion started: 9 September 2025

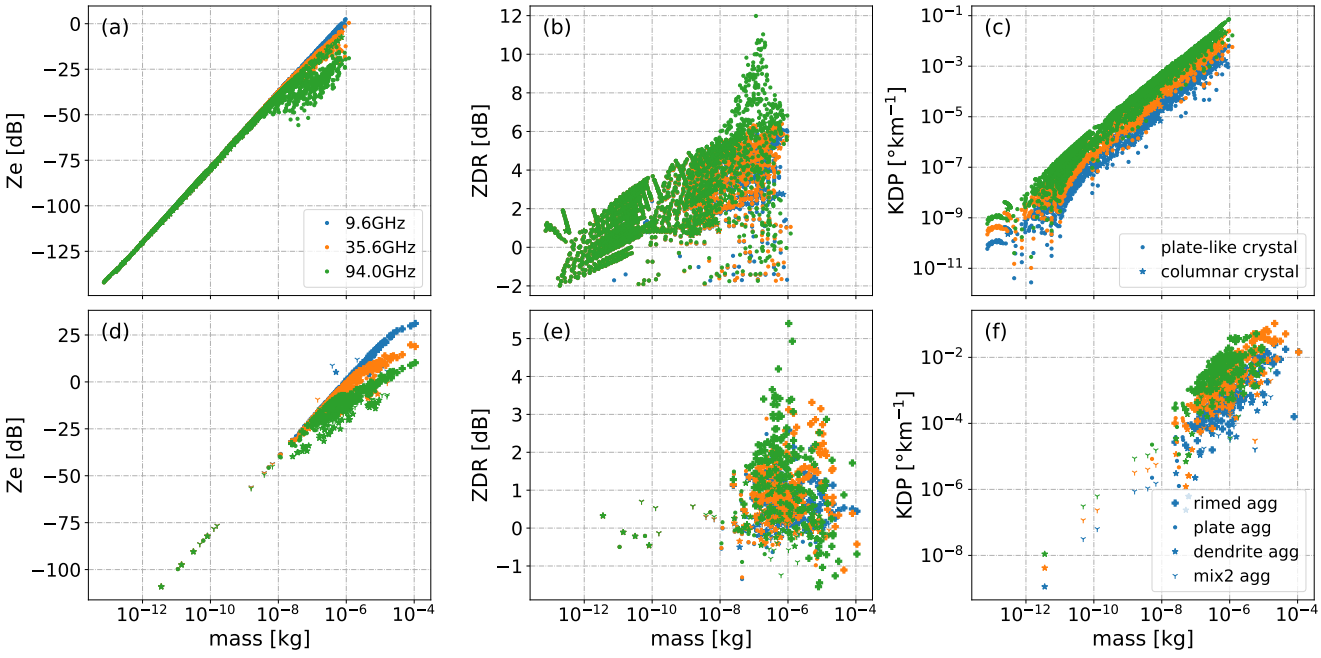

Figure 6. Radar reflectivity (first column), ZDR (second column), and KDP in dependency of the particle mass plotted for all particles in the database at 30° radar elevation averaged over all azimuth orientations at $\beta = 0°$. The first row shows the scattering properties of all ice crystals at 9.6GHz (blue), 35.6GHz (orange) and 94GHz (green). The dots indicate plate-like crystals and the stars columnar crystals. The second row shows the scattering properties of all aggregates at 9.6, 35.6 and 94 GHz. The dots indicate aggregates of plates, the stars aggregates of dendrites, the trident mix2 aggregates, and the plus sign rimed aggregates.

4.1 Radar Simulator McRadar

McRadar is a flexible radar forward simulator designed to interface directly with the level 1b LUTs and forward simulate microphysical model output into radar observables while maintaining consistency in physical properties. Similar to existing forward operators such as the Cloud-resolving model Radar SIMulator CR-SIM (Oue et al., 2020), McRadar calculates the Doppler spectrum, specific differential phase shift (KDP), and attenuation based on the microphysical inputs. Instrument-specific noise can be added to the Doppler spectra, and spectral broadening effects due to turbulence, finite beamwidth, and wind shear are optionally included following Doviak and Zrnic (1993).

McRadar also allows the user to specify particle canting angle distributions (e.g., wobbling), enabling more realistic simulations. From the Doppler spectra, standard radar moments, including equivalent reflectivity (Z_e), mean Doppler velocity, differential reflectivity (ZDR), KDP, and linear depolarization ratio (LDR), are derived.

Allowing the ice particle to grow via deposition, during which the shape of the particle evolves using a habit prediction (Welss et al., 2024), results in a multitude of particle shapes, and therefore a large variability of particle size, mass, and aspect ratio for which scattering properties need to be found. To find the scattering properties of a particle that best fits with its microphysical

https://doi.org/10.5194/egusphere-2025-3910
Preprint. Discussion started: 9 September 2025

properties (i.e., mass, size, and aspect ratio) to the model-predicted particle, McRadar performs a nearest-neighbour selection or regression on the level 1b LUTs, depending on user preference. This is implemented using the `scikit-learn` Python library, which supports efficient neighbour search algorithms. By default, McRadar uses neighbours-based regression, where the output is a weighted average of the n nearest neighbours based on inverse distance to the query point. This supervised learning approach follows the methodology described by Roweis et al. (2004), and more details can be found in the official documentation: https://scikit-learn.org/1.5/modules/neighbors.html.

For monomers, the scattering properties are retrieved using the nearest match in mass, $D_{\max}$, and aspect ratio in logarithmic space. For aggregates, the nearest match is found based on mass and $D_{\max}$ in logarithmic space.

4.1.1 Validation of Nearest Neighbour Lookup

To validate the accuracy of the nearest-neighbour selection method, we performed a cross-validation test by randomly removing individual data points from the database. For 1,000 such points, we used the nearest-neighbour method to estimate the Mueller and amplitude matrix entries, which were then compared against the true values.

We specifically evaluated the backscattering cross sections at horizontal and vertical polarization ($c_{\mathrm{bck},hh}$ and $c_{\mathrm{bck},vv}$), ZDR, and KDP at 94 GHz and 30° elevation, using different values of n (number of neighbours). As shown in Figure 7, the retrieved values exhibit a high correlation with the true values and no evident bias. Among the radar variables, ZDR shows the largest scatter.

Table 1 presents a statistical summary of the validation. Correlation coefficients for all matrix entries and radar variables range from 0.8 to 0.98, indicating high retrieval fidelity. Notably, $c_{\mathrm{bck},vv}$ has the lowest correlation, while $c_{\mathrm{bck},hh}$ shows the highest. The variability in ZDR is likely a result of the lower correlation in $c_{\mathrm{bck},vv}$.

However, because radar measurements always involve ensembles of particles (even within a single Doppler bin), small deviations in individual particle properties are acceptable, provided that no systematic bias exists in the retrievals.

5 Application examples

This database has two key advantages: First, it allows for consistent forward simulation of the radar signatures of frozen particles with strongly varying microphysical properties. Second, the large number of particles likely reduces a bias introduced by considering a single particle to be representative of all particles with a certain size or mass. As shown in Fig. 6, especially the polarimetric scattering properties for one particle with a specific mass can span several orders of magnitude. Choosing a single particle per mass/size to represent all particles close to that mass/size proves difficult and might cause a significant bias, as was also shown in Ori et al. (2021). We want to illustrate these two advantages with two application examples which are presented in the following sections.

https://doi.org/10.5194/egusphere-2025-3910
Preprint. Discussion started: 9 September 2025

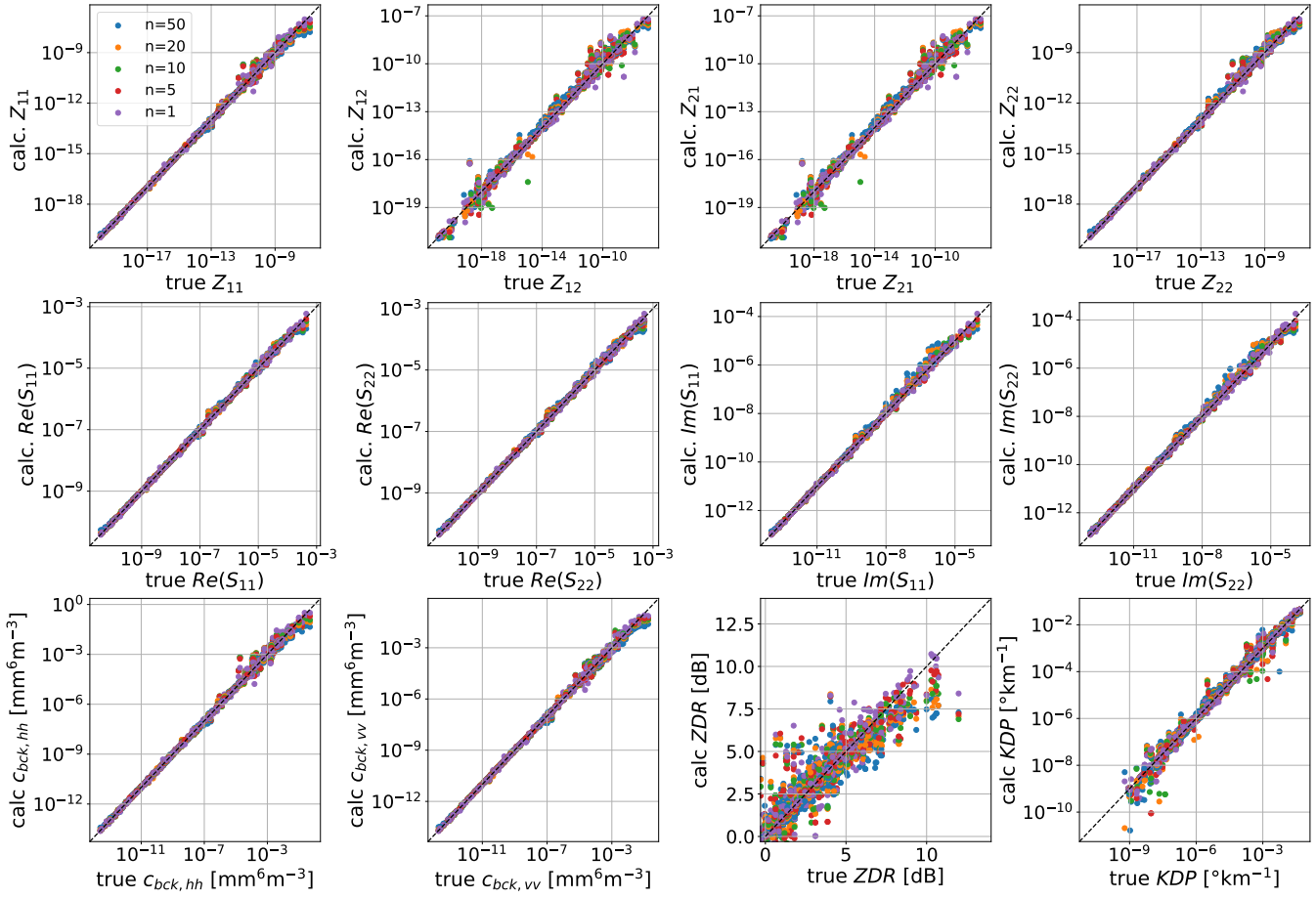

Figure 7. Result of the validation of the nearest neighbour selection from the scattering database. Shown are scatter plots of the true values and calculated values at 94GHz and 30° elevation. The first row shows the entries of the Mueller matrix, the second row of the Amplitude matrix, the third row of the calculated reflectivity at horizontal and vertical polarization, ZDR, and KDP.

5.1 Simulated radar quantities of single growing ice crystals

Showing the flexibility of the DDA database in terms of large variability of particle properties is done by forward simulating the trajectories (or growth histories) of ice crystals that are sedimenting towards the ground while growing through deposition. The habit of ice crystals strongly depends on the ambient temperature and super-saturation (i.e. Bailey and Hallett, 2009). Recently, a habit prediction has been implemented in the Lagrangian Monte-Carlo particle model McSnow (Welss et al., 2024). The habit of an ice crystal can be described by its aspect ratio ϕ. In McSnow, ϕ is defined as the ratio of the c to the a-axis $\phi = \frac{c}{a}$, where the a-axis is the maximum dimension of the basal face, and the c-axis is the maximum dimension of the prism face. The

https://doi.org/10.5194/egusphere-2025-3910
Preprint. Discussion started: 9 September 2025

	n	1	5	10	20	50
$c_{bck,hh}$ [$\mathrm{mm^6 m^{-3}}$]	mean error	9.60×10^{-4}	9.25×10^{-4}	1.06×10^{-3}	1.24×10^{-3}	1.45×10^{-3}
	median error	3.99×10^{-10}	2.50×10^{-10}	3.40×10^{-10}	3.13×10^{-10}	4.77×10^{-10}
	correlation coefficient	0.94	0.91	0.90	0.87	0.84
	bias	1.97×10^{-4}	2.58×10^{-4}	3.36×10^{-4}	3.72×10^{-4}	4.14×10^{-4}
$c_{bck,vv}$ [$\mathrm{mm^6 m^{-3}}$]	mean error	6.91×10^{-4}	$6.26 \times 10{-4}$	7.38×10^{-4}	7.58×10^{-4}	8.28×10^{-4}
	median error	2.06×10^{-10}	1.11×10^{-10}	8.39×10^{-11}	1.28×10^{-10}	1.63×10^{-10}
	correlation coefficient	0.84	0.84	0.79	0.79	0.77
	bias	7.09×10^{-5}	8.57×10^{-5}	9.57×10^{-5}	1.02×10^{-4}	1.16×10^{-4}
ZDR [dB]	mean error	0.35	0.43	0.52	0.59	0.72
	median error	0.11	0.16	0.21	0.26	0.36
	correlation coefficient	0.94	0.93	0.91	0.90	0.88
	bias	-0.25	-0.84	-1.20	-1.20	-1.13
KDP [$^\circ\mathrm{km^{-1}}$]	mean error	2.18×10^{-4}	2.40×10^{-4}	2.72×10^{-4}	3.23×10^{-4}	3.84×10^{-4}
	median error	7.31×10^{-8}	6.28×10^{-8}	8.47×10^{-8}	1.05×10^{-7}	1.63×10^{-7}
	correlation coefficient	0.97	0.97	0.97	0.96	0.96
	bias	-8.91×10^{-7}	1.80×10^{-6}	3.37×10^{-6}	4.52×10^{-6}	6.44×10^{-6}

Table 1. The mean error, median error, standard deviation of the error as well as the correlation and bias between the true backscattering cross sections at horizontal and vertical polarization, the true ZDR, the true KDP and the calculated backscattering cross sections, ZDR and KDP.

change of ϕ can be calculated with

$$\frac{\mathrm{dc}}{\mathrm{d}a} = \mathrm{d}\phi = \frac{\alpha_\mathrm{c}(T)}{\alpha_\mathrm{a}(T)}\phi = \Gamma(T)\phi \tag{11}$$

with the deposition coefficients of axis c (α_c) and axis a (α_a) and the temperature (T) dependent inherent growth function Γ. Γ has been determined by different studies through comparison with observational data as well as laboratory experiments (i.e. Welss et al., 2024; Chen and Lamb, 1994). The change of mass due to depositional growth can then be calculated with the well-known mass growth equation (i.e. Lohmann et al., 2016, Chapter 7)

$$\frac{\mathrm{d}m}{\mathrm{d}t} = 4\pi C D_\mathrm{v} \bar{f} \frac{S_i - 1}{F_\mathrm{k}^i + F_\mathrm{d}^i} \tag{12}$$

with the mass of the particle m, the water vapour diffusivity D_v, ambient saturation ratio with respect to ice S_i, particle ventilation coefficient $\bar{f}$. F_k^i, describes the latent heat release due to sublimation and the diffusion of heat away from the ice particle, and F_d^i describes the diffusion of water vapour towards the ice particle. They are expressed as

$$F_\mathrm{k}^i = \left(\frac{L_\mathrm{s}}{R_\mathrm{v}T} - 1\right); \quad F_\mathrm{d}^i = \frac{R_\mathrm{v}T}{D_\mathrm{v} e_{\mathrm{s,i}}(T)} \tag{13}$$

With L_s the latent heat of sublimation, T the ambient temperature, R_v the gas constant of water vapour and $e_{\mathrm{s,i}}(T)$ the saturation vapour pressure above ice at the temperature T.

https://doi.org/10.5194/egusphere-2025-3910
Preprint. Discussion started: 9 September 2025

The change of ϕ is taken into account through the capacity C (with subscript p for plate-like particles, c for columnar particles):

$$C_p = \frac{\alpha \epsilon_\mathrm{p}}{\sin^{-1}(\epsilon_\mathrm{p})}; \quad C_c = \frac{c \epsilon_\mathrm{c}}{\ln(1+\epsilon_c)\phi} \tag{14}$$

with $\epsilon_\mathrm{p} = \sqrt{1-\phi^2}$ and $\epsilon_\mathrm{c} = \sqrt{1-\phi^{-2}}$.

An additional variable necessary to determine the habit of an ice crystal is its overall density. This density is, for example, reduced from solid ice density through branching of dendrites at temperatures close to $-15\ ^\circ C$ or hollowing of columns at temperatures between -5 and $-10\ ^\circ C$. In McSnow, the volume enveloping ice crystals is simulated as a spheroid, which does not allow to simulate branching or hollowing directly. Instead, the density of the spheroid is adapted by amplifying the increase of the ice volume V relative to the mass m.

$$\frac{\mathrm{d}V}{\mathrm{d}t} = \frac{1}{\rho_\mathrm{depo}} \frac{\mathrm{d}m}{\mathrm{d}t} \tag{15}$$

The deposition density ρ_{depo} depends on the ambient temperature and is proportional to $\rho_i \Gamma(T)$ for plate-like particles and $\rho_i \Gamma(T)^{-1}$ for columnar particles with ice density ρ_i. For further details about the habit prediction, the reader is referred to Welss et al. (2024).

For this application, the modified inherent growth function (IGF2) from Welss et al. (2024) has been used. While McSnow is a Lagrangian Monte-Carlo particle model, designed to simulate populations of particles, it is also possible to simulate the evolution of single ice particles due to various microphysical processes, in this case depositional growth and sedimentation. Keeping the ambient super-saturation with respect to ice constant at 5%, setting the temperature at the ground to 0 ° C and assuming a constant lapse rate of 6 K km^{-1}, 5 particles were simulated starting at different heights (temperatures). The particles were initialized with a diameter of $10\ \mu$m and an aspect ratio of unity. During the simulation, the particles grow by deposition as predicted by the habit prediction while sedimenting through different temperature regimes towards the ground. No interactions between the particles have been assumed.

Depending on the temperature at which a particle was initialized, the physical properties vary significantly (see Fig. 8). The particles that started at temperatures colder than -22 ° C are growing columnar (with an aspect ratio larger than 1), while the particles initialized at temperatures warmer than -22 ° C grow plate-like (with an aspect ratio smaller than 1). The particle that was initialized at -15 ° C experiences the strongest depositional growth, reaching a maximum dimension (D_{max}) of 3.5 mm and an aspect ratio of 0.0015, consistent with laboratory studies (Pruppacher and Klett, 1997). The density of this particle is significantly reduced, reaching a minimum of 390 kg m^{-3}. This indicates significant branching, as is expected by the predominantly dendritic growth at -15 ° C. The smallest mass and D_{max} is reached by the particle nucleated at -10 ° C. This particle initially grows plate-like, but is sedimenting out of the plate growth region into the columnar growth region at temperatures warmer than -10 ° C. Therefore, the particle only slowly increases its mass and D_{max} while at the same time increasing its aspect ratio toward unity.

This large variability of ice microphysical properties produced by the McSnow simulation highlights the need for a scattering database consisting of ice particles with a similar variability. For the database in this study, we therefore generated specific ice

https://doi.org/10.5194/egusphere-2025-3910
Preprint. Discussion started: 9 September 2025

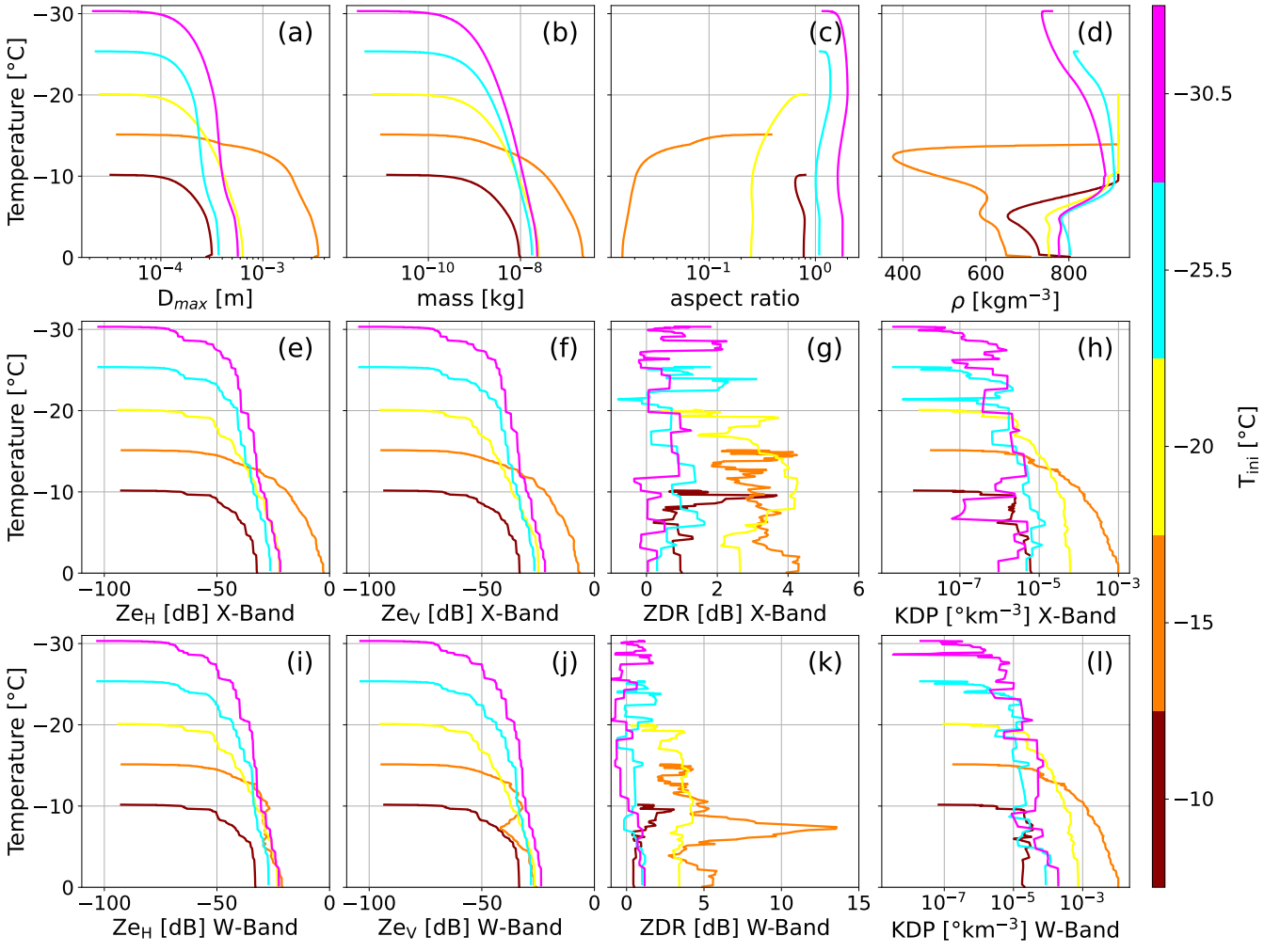

Figure 8. First row: Microphysical properties of single ice crystals nucleated at different temperatures and growing by deposition using the habit prediction (Welss et al., 2024) while sedimenting towards the ground. Shown are the evolution of the maximum dimension D_{max} (a), mass (b), aspect ratio (c) and density ρ (d) with ambient temperature. The second row shows the corresponding radar forward simulations for each particle at 94 GHz and 30° elevation. Shown are the single particle reflectivity Ze at horizontal (e) and vertical (f) polarization, the single particle ZDR (g), and the single particle KDP (h).

crystals that can provide this large variability in ice microphysical properties. The corresponding forward simulations using the nearest-neighbour regression with $n = 10$ to access the DDA LUTs, are shown in the second and third row of Fig. 8.

The most interesting scattering properties are expected from particles nucleated within the dendritic growth zone (between -10 and -20 ° C). Those particles experience the strongest depositional growth, and reduce their density through branching. While growth effects such as branching can be seen in a reduction of ZDR, e.g. at -14.2 ° C for the particle nucleated at -15 ° C, also differences at different frequencies can be observed. While at X-Band, ZDR of the particle nucleated at -15 ° C

https://doi.org/10.5194/egusphere-2025-3910
Preprint. Discussion started: 9 September 2025

only slightly increases towards warmer temperatures, at W-Band a strong peak at -8 ° C is observed, where a ZDR of 14.5 dB is reached. Looking at the single particle scattering properties in Figure 6, it is evident that particles with a mass between 10^{-8} and 10^{-6} kg are producing large ZDR at W-Band. This mass corresponds to approximately a D_{max} of 3 mm, which is close to the wavelength of W-band, causing non-Rayleigh scattering effects. While both ZeH and ZeV are in the non-Rayleigh regime (ZeH and ZeV are not increasing as fast at W-Band as at X-Band), ZeV is affected stronger than ZeH, causing the large increase in ZDR.

In-situ observations sometimes reveal particles which must have grown in multiple growth regimes (Bailey and Hallett, 2009). For example, capped-columns are observed when an ice crystal initially grows columnar, then sediments into the plate-like growth regime and develops plates on both ends of the column. In this simulation, the particle nucleated at -25 ° C could potentially develop as a capped column in nature. In the model, these kinds of particles are, however, not represented. Only the change in aspect ratio and density of the particle can be captured. The transition from the columnar to the plate-like growth regime causes a reduction of the aspect ratio towards unity. While the addition of capped-columns is in principle possible, we have decided not to include these particles in the scattering database, as this introduces the need to include the growth history of the ice particle in the forward simulations. Rather, in the database, we have generated plates, dendrites, and columns with aspect ratios close to unity. In Bailey and Hallett (2009), it has also been shown in a laboratory study, that when a column transitions into the plate-like growth regime, under certain circumstances it can also just reduce its aspect ratio rather than producing a plate at each end, which might justify our approach.

5.2 Simulated radar signatures of idealized 1D McSnow simulation

Previous scattering databases often limited the number of ice particles due to the high computational costs of the DDA. For example, the database of Brath et al. (2020) contains 51 plate-like ice crystals and 18 aggregates. These particles are then treated as representative of all ice particles with a given size or mass. In reality, microphysical properties can vary substantially for a given maximum dimension (D_{max}) or mass, introducing significant uncertainty, and potentially even bias, into the calculated scattering properties. Ori et al. (2021) demonstrated this uncertainty by comparing the scattering properties of a single particle to those of a large ensemble of particles with similar sizes.

But how significant might be the impact in forward simulated radar variables of always using the scattering properties of the closest fitting particle versus using average scattering properties of particles in the vicinity of the properties needed? Because we needed to generate a wide variety of particle properties to account for the particle variability in McSnow, our scattering database includes a larger number of ice particles, but with a limited number of frequencies included. This enables us to test the effect of using single versus averaged particle scattering properties for each D_{max}, mass, and aspect ratio retrieved from the database.

To investigate potential biases arising from particle representation, we performed an idealized one-dimensional simulation using McSnow. McSnow is particularly well-suited for this purpose, as it explicitly simulates the microphysical evolution of individual particles. For this case study, we adopt the same atmospheric setup as in Section 5.1: a surface temperature of 0 ° C, a lapse rate of 6 K km^{-1}, and a constant relative humidity with respect to ice of 105%. Ice particles are initialized in a nucleation

https://doi.org/10.5194/egusphere-2025-3910
Preprint. Discussion started: 9 September 2025

layer spanning 2–6 km altitude, corresponding to temperatures from –10 ° C to –30 ° C. In this layer, we assume a constant nucleation rate of 0.375 particles $s^{-1}m^{-3}$, leading to a maximum concentration of 2000 particles m^{-3} at -15 ° C.

During the simulation, ice particles may grow by deposition and aggregation. Since we use the temperature-dependent sticking efficiency from Connolly et al. (2012), aggregation becomes an important growth mechanism only at temperatures warmer than -20 ° C. In the current McSnow setup, aggregates follow predefined mass–size and area–size relationships; here, we assume aggregates composed of side planes, columns, and bullet rosettes as described in Mitchell et al. (1996).

For our reference radar forward simulation, we use the 10 nearest neighbours to estimate the scattering properties of each simulated super-particle. The simulated radar variables are shown in the first row of Figure 9.

5.2.1 Microphysical evolution

The idealized McSnow simulation exhibits radar signatures commonly observed in the field, as reported for example by von Terzi et al. (2022) and references therein. A continuous increase in Ze toward the ground, accompanied by a rise in DWR, is a strong indicator of intensifying aggregation. Also in the Doppler spectra, aggregation leads to a rapidly increasing spectral Ze at a temperature close to -15 ° C. The aggregation of fast-falling columnar ice crystals leads to a lower fall velocity of the resulting aggregates with larger reflectivities. A second mode in the spectrum in this temperature region can be explained by nucleation of ice particles, which grow into dendrites that have low fall velocities due to their large cross-sectional area. Together, these processes cause the prominent dip in the MDV close to -15 ° C.

The dendritic ice crystals also produce characteristic polarimetric signatures. KDP begins to increase slightly at around -30 ° C, followed by a strong increase at -18 ° C, reaching a maximum of 0.55 ° km^{-1} in the dendritic growth layer at -15 ° C. This height also coincides with a small peak in ZDR. Also at -18 ° C, $sZDR_{max}$ begins to increase, reaching values up to 5 dB at-15 ° C. Below this layer, toward the ground, all polarimetric variables decrease slightly, reflecting the aggregation of the largest dendritic ice crystals.

5.2.2 Single versus averaged particle scattering properties

The identical McSnow output was forward simulated once with using only the scattering properties of the particle which fits the super-particle the best (nearest-neighbour, n=1, second row in Figure 9) and a second time using the average scattering properties of the 10 particles being closest with their physical properties to the super-particle (Figure 9, first row).

The difference plots (Figure 9, third row) indicate that some radar variables are more sensitive than others to the variability in the scattering properties of individual particles. Ze and MDV are largely unaffected, with maximum differences of only –3 dB and 0.02 ms^{-1}, respectively, between the reference simulation and the n=1 case. DWR and KDP show a larger sensitivity. For example, at temperatures warmer than –12 ° C, DWR_{KaW} is increasingly underestimated, reaching a maximum underestimation of 2.2 dB at 0 ° C.

The strongest effect of using n=1 for ice crystals is visible in the Doppler spectrum as well as in KDP and $sZDR_{max}$. In the simulation with n=1, the spectral Ze of dendritic particles near -15 ° C is strongly overestimated, by 5–7 dB. Interestingly, this overestimation in Ze does not translate into large differences in $sZDR_{max}$ at the same temperature. However, at temperatures

https://doi.org/10.5194/egusphere-2025-3910
Preprint. Discussion started: 9 September 2025

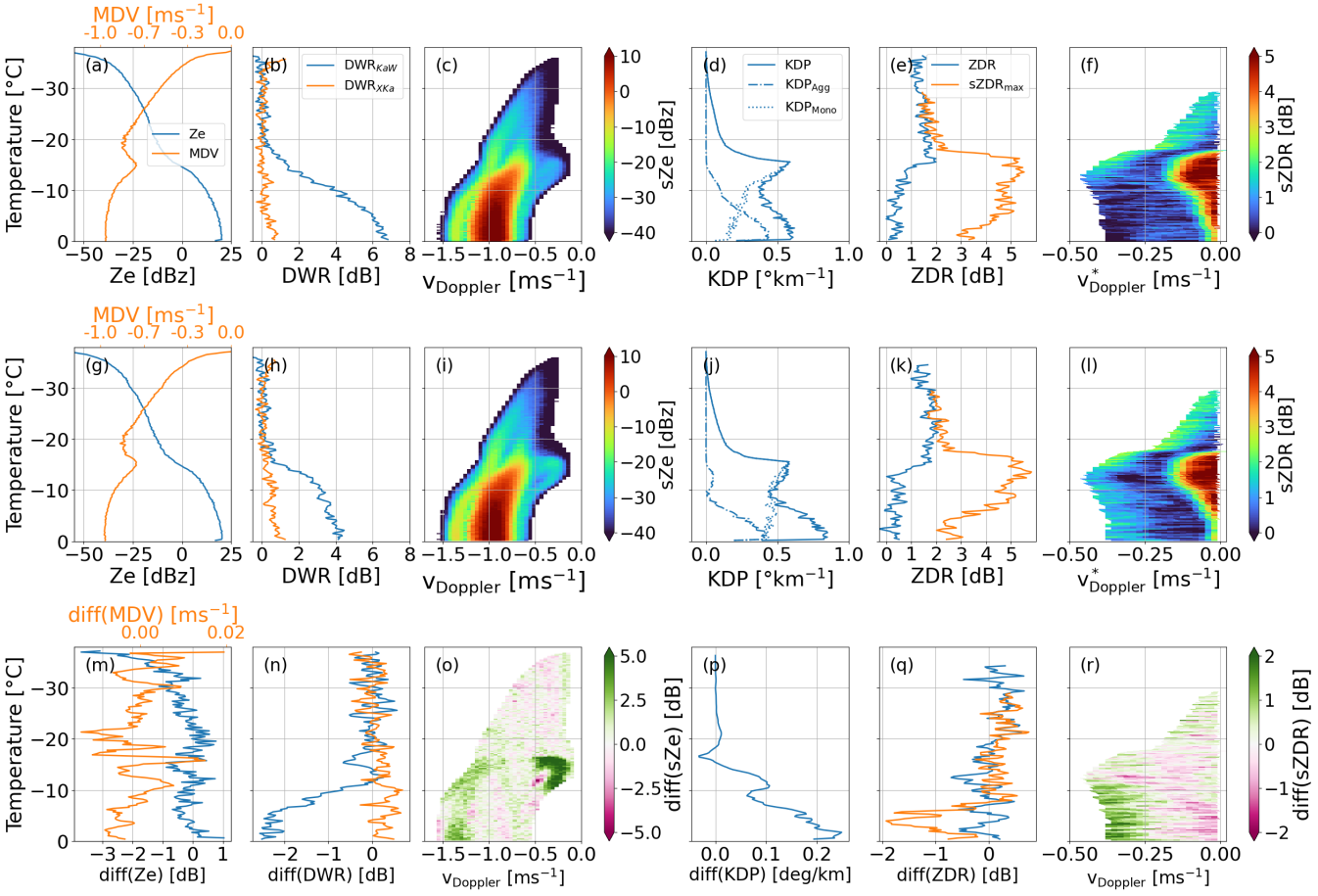

Figure 9. Impact of using single or averaged particle scattering properties demonstrated with 1D McSnow simulations of an idealized cloud: The reference simulation using the averaged scattering properties of 10 particles for each super-particle in the forward simulation is shown in the first row. The second row contains the forward simulation with the scattering properties of only one particle per super-particle. The third row shows the difference between row 2 and row 1. The different columns display Ze, MDV at Ka-Band and 90° elevation (first column), $\mathrm{DWR_{KaW}}$, and $\mathrm{DWR_{XKa}}$ at 90° elevation (second column), spectral Ze at Ka-Band and 90° elevation (third column), KDP at W-Band and 30° elevation (fourth column), ZDR as well as the maximum of spectral ZDR at W-band and 30° elevation (fifth column) and spectral ZDR at W-band and 30° elevation (sixth column).

warmer than –8 ° C, $\mathrm{sZDR_{max}}$ is increasingly underestimated, by up to 2 dB. Similarly, the selected ice crystals strongly affect KDP, which shows an increasing overestimation toward warmer temperatures. The largest overestimation appears near 0 ° C, where KDP is overestimated by 2.2 ° km^{-1}. This bias is primarily driven by the ice crystal population; for aggregates, KDP even shows a slight underestimation.

https://doi.org/10.5194/egusphere-2025-3910
Preprint. Discussion started: 9 September 2025

These results clearly demonstrate that biases arise when a single particle is assumed to represent all particles of a given size or mass. Interestingly, the bias is not consistent in direction. For example, in the same temperature range, KDP is overestimated while $sZDR_{max}$ is underestimated. Likewise, while sZe is strongly overestimated, no corresponding bias is seen in $sZDR_{max}$.

Clearly, the magnitude and nature of these biases depend on the specific simulation setup. This sensitivity experiment was designed to illustrate the potential differences between ensemble-averaged scattering properties and single-particle scattering properties. Determining which approach more accurately reflects reality, however, cannot be resolved within the scope of this study.

6 Summary and conclusions

New developments in microphysical models, such as Lagrangian particle models including a habit prediction for ice particles or the P3 scheme (Morrison et al., 2025), which continuously evolves the microphysical properties of ice particles, necessitate a scattering database that can cope with largely varying microphysical properties. In this study, we have presented a new DDA scattering database consisting of 2600 ice crystals, including a large variation of dendritic ice crystals, plates, columns, and needles, as well as 450 aggregates of plates, dendrites, mixed monomer habits, and various degrees of riming. The scattering properties of these particles at C-, X-, Ka-, and W-Band at various elevation and azimuth angles, as well as orientationally averaged scattering properties, are available. The database is structured on three levels. Level 0 comprises the raw ADDA output (including the Mueller and Amplitude matrices) for each wavelength, elevation, and azimuth orientation. level 1a summarizes the for radar applications relevant Mueller and Amplitude matrix entries for each particle type in netcdf files. level 1b consists of the averages of azimuthally random orientations of all particles summarized in LUTs. These LUTs can be accessed via the radar simulator McRadar, where radar Doppler spectra at horizontal and vertical polarization as well as KDP are simulated, or interfaced to other forward operators.

In this study, we have demonstrated the two main advantages of this database: First, due to the large variety of realistic ice crystals available, this database can be utilized to forward simulate complex model output, where the ice particle habit is predicted. This enables us to study depositional growth signatures of ice crystals that could be expected, for example, in the dendritic growth layer. Second, using realistically shaped ice particles in forward simulations always poses the challenge of choosing the "correct" shape of ice particle. This shape has a significant influence on the scattering properties and can thus cause a bias in forward simulations (Ori et al., 2021). This database is based on a large number of ice particles, allowing to consider the scattering properties of multiple ice particles for each forward simulated particle, which might reduce the bias introduced by choosing the wrong shape of ice particles.

While the focus of the database thus far was placed on dendritic ice crystals, current developments in McSnow shift our focus to aggregate properties. Therefore, in the near future, the database will be expanded by the scattering properties of a large ensemble of aggregates.

https://doi.org/10.5194/egusphere-2025-3910
Preprint. Discussion started: 9 September 2025

Code and data availability. The paper presents the new DDA database, level 1a and level 1b, which are archived on zenodo under the terms of the Creative Commons Attribution 4.0 Internationals licence (https://doi.org/10.5281/zenodo.16792943, von Terzi et al., 2025). This study introduced the radar forward operator McRadar, which is released under the terms of the 3-clause BSD licence and available at https://github.com/lterzi/McRadar, the exact version of McRadar used for this publication is archived on zenodo under (https://doi.org/10.5281/zenodo.17079541, von Terzi, 2025b). All codes used to generate the ice crystals, calculate the scattering properties and produce the Figures can be found in https://github.com/lterzi/DDA_database_gmd, archived on zenodo under (https://doi.org/10.5281/zenodo.17079588, von Terzi, 2025a).

Appendix A: Scattering properties of all particles depending on D_{max}

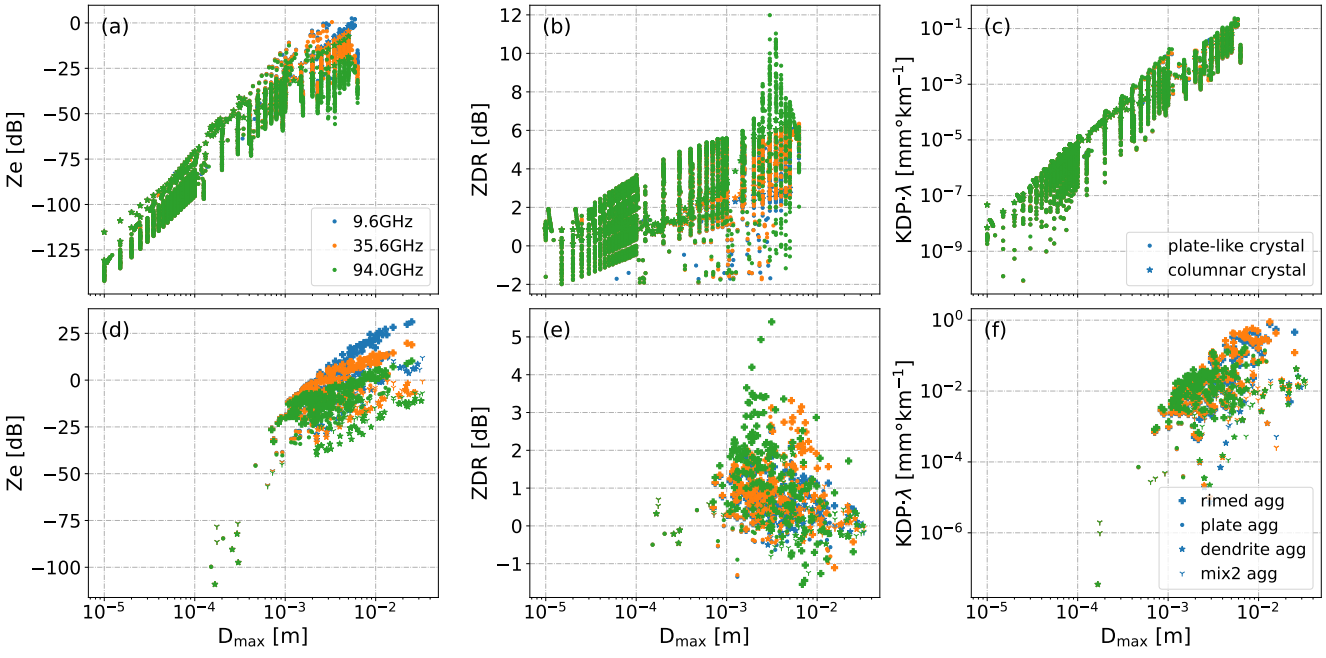

Figure A1. As Figure 6, but in dependency of the maximum dimension D_{max} instead of mass. KDP is normalized with the wavelength to allow an easier comparison with Figure C1 of von Terzi et al. (2022)

Appendix B: Uncertainty analysis of the selection from the Look-up tables

https://doi.org/10.5194/egusphere-2025-3910
Preprint. Discussion started: 9 September 2025

	$n_{neighbours}$	5	10	20	50
Z_{11}	mean error	2.13×10^{-4}	2.37×10^{-4}	2.46×10^{-4}	3.05×10^{-4}
	median error	3.70×10^{-11}	5.79×10^{-11}	4.48×10^{-11}	5.54×10^{-11}
	correlation coefficient	0.89	0.77	0.75	0.73
	bias	2.02×10^{-5}	2.25×10^{-5}	2.41×10^{-5}	2.72×10^{-5}
Z_{12}	mean error	1.08×10^{-4}	1.26×10^{-4}	1.40×10^{-4}	1.61×10^{-4}
	median error	3.08×10^{-11}	3.71×10^{-11}	$4.06 \times 10^{-11}0$	6.11×10^{-11}
	correlation coefficient	0.98	0.97	0.95	0.87
	bias	7.95×10^{-6}	8.80×10^{-6}	9.35×10^{-6}	9.74×10^{-6}
Z_{21}	mean error	1.08×10^{-4}	1.26×10^{-4}	1.40×10^{-4}	1.61×10^{-4}
	median error	3.08×10^{-11}	3.71×10^{-11}	4.06×10^{-11}	6.11×10^{-11}
	correlation coefficient	0.98	0.97	0.95	0.87
	bias	7.95×10^{-6}	8.80×10^{-6}	9.35×10^{-6}	9.74×10^{-6}
Z_{22}	mean error	2.13×10^{-4}	2.37×10^{-4}	2.46×10^{-4}	3.05×10^{-4}
	median error	3.70×10^{-11}	5.79×10^{-11}	4.48×10^{-11}	5.54×10^{-11}
	correlation coefficient	0.89	0.77	0.75	0.73
	bias	2.02×10^{-5}	2.25×10^{-5}	2.41×10^{-5}	2.72×10^{-5}

Table B1. Same as Table 1 but for the entries of the Mueller Matrix relevant for radar applications

https://doi.org/10.5194/egusphere-2025-3910
Preprint. Discussion started: 9 September 2025

	$n_{neighbours}$	5	10	20	50
$Re(S_{11})$	mean error	1.04×10^{-3}	1.23×10^{-3}	1.63×10^{-3}	2.37×10^{-3}
	median error	1.63×10^{-7}	1.65×10^{-7}	1.56×10^{-7}	2.23×10^{-7}
	correlation coefficient	0.99	0.98	0.97	0.94
	bias	4.06×10^{-4}	5.20×10^{-4}	7.16×10^{-4}	9.76×10^{-4}
$Re(S_{22})$	mean error	1.91×10^{-3}	2.31×10^{-3}	2.99×10^{-3}	3.81×10^{-3}
	median error	2.52×10^{-7}	3.82×10^{-7}	5.39×10^{-7}	6.32×10^{-7}
	correlation coefficient	0.99	0.98	0.97	0.95
	bias	7.31×10^{-4}	1.01×10^{-3}	1.26×10^{-3}	1.83×10^{-3}
$Im(S_{11})$	mean error	1.93×10^{-4}	2.05×10^{-4}	2.47×10^{-4}	3.62×10^{-4}
	median error	5.47×10^{-10}	5.28×10^{-10}	4.57×10^{-10}	6.56×10^{-10}
	correlation coefficient	0.94	0.93	0.91	0.86
	bias	1.63×10^{-5}	1.92×10^{-5}	2.44×10^{-5}	2.95×10^{-5}
$Im(S_{22})$	mean error	4.29×10^{-4}	4.87×10^{-4}	6.23×10^{-4}	7.62×10^{-4}
	median error	1.13×10^{-9}	1.74×10^{-9}	1.98×10^{-9}	2.85×10^{-9}
	correlation coefficient	0.94	0.92	0.89	0.84
	bias	4.39×10^{-5}	5.32×10^{-5}	6.08×10^{-5}	7.24×10^{-5}

Table B2. Same as Table 1 but for the entries of the Amplitude matrix relevant for radar applications

Author contributions. LvT generated the ice particles, performed the scattering calculations and provided the application examples. LvT and DO contributed to the radar forward operator. DO performed the averages over the azimuthally random oriented particles. SK acquired funding and guided the research project. All authors contributed to the text. The AI tool chatGPT was used to correct spelling and improve readability of the text.

Competing interests. The authors declare that they have no competing interests.

Acknowledgements. Contributions by L. von Terzi, S. Kneifel and D. Ori have been funded by the Deutsche Forschungsgemeinschaft (DFG, German Research Foundation) Priority Program SPP2115 “Fusion of Radar Polarimetry and Numerical Atmospheric Modelling Towards an Improved Understanding of Cloud and Precipitation Processes" (PROM), projects “Exploring the role of FRAGmentation of ice particles by combining super-partIcle modelling, Laboratory studies, and polarimEtric radar observations" (FRAGILE, project number 492234709) and “Polarimetric Radar simulations with realistic Ice and Snow properties and mulTI-frequeNcy consistency Evaluation" (PRISTINE project number 492274454). We would like to thank Dr. Axel Seifert and Dr. Christoph Siewert for their valuable help with McSnow. We would further like to thank Dr. Fabian Jakub for helpful discussions concerning the setup of the look-up tables.

https://doi.org/10.5194/egusphere-2025-3910
Preprint. Discussion started: 9 September 2025

References

Bailey, M. and Hallett, J.: Growth rates and habits of ice crystals between -20°C and -70°C, Journal of the Atmospheric Sciences, 61, 514–544, https://doi.org/10.1175/1520-0469(2004)061<0514:GRAHOI>2.0.CO;2, 2004.

Bailey, M. P. and Hallett, J.: A comprehensive habit diagram for atmospheric ice crystals: Confirmation from the laboratory, AIRS II, and other field studies, Journal of the Atmospheric Sciences, 66, 2888–2899, https://doi.org/10.1175/2009JAS2883.1, 2009.

Brath, M., Ekelund, R., Eriksson, P., Lemke, O., and Buehler, S. A.: Microwave and submillimeter wave scattering of oriented ice particles, Atmospheric Measurement Techniques, 13, 2309–2333, https://doi.org/10.5194/amt-13-2309-2020, 2020.

Chen, J.-P. and Lamb, D.: The theoretical basis for the parameterization of ice crystal habits: Growth by vapor deposition, Journal of Atmospheric Sciences, 51, 1206–1222, https://doi.org/10.1175/1520-0469(1994)051<1206:TTBFTP>2.0.CO;2, 1994.

Connolly, P. J., Emersic, C., and Field, P. R.: A laboratory investigation into the aggregation efficiency of small ice crystals, Atmospheric Chemistry and Physics, 12, 2055–2076, https://doi.org/10.5194/acp-12-2055-2012, 2012.

Doviak, R. J. and Zrnic, D. S.: Doppler radar & weather observations, Academic press, https://doi.org/https://doi.org/10.1016/C2009-0-22358-0, 1993.

Draine, B. T. and Flatau, P. J.: Discrete-dipole approximation for scattering calculations, Journal of the Optical Society of America A, 11, 1491–1499, https://doi.org/10.1364/JOSAA.11.001491, 1994.

Geer, A. J., Lonitz, K., Weston, P., Kazumori, M., Okamoto, K., Zhu, Y., Liu, E. H., Collard, A., Bell, W., Migliorini, S., et al.: All-sky satellite data assimilation at operational weather forecasting centres, Quarterly Journal of the Royal Meteorological Society, 144, 1191–1217, https://doi.org/10.1002/qj.3202, 2018.

Harrington, J. Y., Sulia, K., and Morrison, H.: A Method for Adaptive Habit Prediction in Bulk Microphysical Models. Part I: Theoretical Development, Journal of the Atmospheric Sciences, 70, 349–364, https://doi.org/10.1175/JAS-D-12-040.1, 2013.

Heymsfield, A., Bansemer, A., Wood, N. B., Liu, G., Tanelli, S., Sy, O. O., Poellot, M., and Liu, C.: Toward improving ice water content and snow-rate retrievals from radars. Part II: Results from three wavelength radar–collocated in situ measurements and CloudSat–GPM–TRMM radar data, Journal of Applied Meteorology and Climatology, 57, 365–389, https://doi.org/10.1175/JAMC-D-17-0164.1, 2018.

Jensen, A. and Harrington, J.: Modeling ice crystal aspect ratio evolution during riming: A single-particle growth model, Journal of the Atmospheric Sciences, 72, 2569–2590, https://doi.org/10.1175/JAS-D-14-0297.1, 2015.

Jensen, A. A., Harrington, J. Y., Morrison, H., and Milbrandt, J. A.: Predicting ice shape evolution in a bulk microphysics model, Journal of the Atmospheric Sciences, 74, 2081–2104, https://doi.org/10.1175/JAS-D-16-0350.1, 2017.

Karrer, M., Seifert, A., Siewert, C., Ori, D., von Lerber, A., and Kneifel, S.: Ice particle properties inferred from aggregation modelling, Journal of Advances in Modeling Earth Systems, 12, e2020MS002 066, https://doi.org/10.1029/2020MS002066, 2020.

Kneifel, S., Leinonen, J., Tyynelä, J., Ori, D., and Battaglia, A.: Scattering of hydrometeors, in: Satellite precipitation measurement, pp. 249–276, Springer, https://doi.org/10.1007/978-3-030-24568-9_15, 2020.

Kuo, K.-S., Olson, W. S., Johnson, B. T., Grecu, M., Tian, L., Clune, T. L., van Aartsen, B. H., Heymsfield, A. J., Liao, L., and Meneghini, R.: The microwave radiative properties of falling snow derived from nonspherical ice particle models. Part I: An extensive database of simulated pristine crystals and aggregate particles, and their scattering properties, Journal of Applied Meteorology and Climatology, 55, 691–708, https://doi.org/10.1175/JAMC-D-15-0130.1, 2016.

Leinonen, J. and Moisseev, D.: What do triple-frequency radar signatures reveal about aggregate snowflakes?, Journal of Geophysical Research: Atmospheres, 120, 229–239, https://doi.org/10.1002/2014JD022072, 2015.

https://doi.org/10.5194/egusphere-2025-3910
Preprint. Discussion started: 9 September 2025

Libbrecht, K. G.: Physical dynamics of ice crystal growth, Annu. Rev. Mater. Res, 47, 271–295, https://doi.org/10.1146/annurev-matsci-070616-124135, 2017.

Liu, G.: A database of microwave single-scattering properties for nonspherical ice particles, Bulletin of the American Meteorological Society, 89, 1563–1570, https://doi.org/10.1175/2008BAMS2486.1, 2008.

Locatelli, J. D. and Hobbs, P. V.: Fall speeds and masses of solid precipitation particles, Journal of Geophysical Research (1896-1977), 79, 2185–2197, https://doi.org/10.1029/JC079i015p02185, 1974.

Lohmann, U., Lüönd, F., and Mahrt, F.: An introduction to clouds : from the microscale to climate, Cambridge University Press, Cambridge, https://doi.org/10.1017/CBO9781139087513, 2016.

Lu, Y., Jiang, Z., Aydin, K., Verlinde, J., Clothiaux, E. E., and Botta, G.: A polarimetric scattering database for non-spherical ice particles at microwave wavelengths, Atmospheric Measurement Techniques, 9, 5119–5134, https://doi.org/10.5194/amt-9-5119-2016, 2016.

Maahn, M., Turner, D. D., Löhnert, U., Posselt, D. J., Ebell, K., Mace, G. G., and Comstock, J. M.: Optimal estimation retrievals and their uncertainties: What every atmospheric scientist should know, Bulletin of the American Meteorological Society, 101, E1512–E1523, https://doi.org/10.1175/BAMS-D-19-0027.1, 2020.

Mätzler, C.: Thermal microwave radiation: applications for remote sensing, vol. 52, Iet, https://doi.org/10.1049/PBEW052E, 2006.

McCorquodale, M. W. and Westbrook, C. D.: TRAIL part 2: A comprehensive assessment of ice particle fall speed parametrisations, Quarterly Journal of the Royal Meteorological Society, 147, 605–626, https://doi.org/10.1002/qj.3936, 2021.

Mishchenko, M. I.: Calculation of the amplitude matrix for a nonspherical particle in a fixed orientation, Appl. Opt., 39, 1026–1031, https://doi.org/10.1364/AO.39.001026, 2000.

Mishchenko, M. I. and Yurkin, M. A.: On the concept of random orientation in far-field electromagnetic scattering by nonspherical particles, Optics letters, 42, 494–497, https://doi.org/10.1364/OL.42.000494, 2017.

Mishchenko, M. I., Travis, L. D., and Mackowski, D. W.: T-matrix computations of light scattering by nonspherical particles: A review, Journal of Quantitative Spectroscopy and Radiative Transfer, 55, 535–575, https://doi.org/10.1016/0022-4073(96)00002-7, 1996.

Mitchell, D. L.: Use of Mass- and Area-Dimensional Power Laws for Determining Precipitation Particle Terminal Velocities, Journal of the Atmospheric Sciences, 53, 1710–1723, https://doi.org/10.1175/1520-0469(1996)053<1710:UOMAAD>2.0.CO;2, 1996.

Mitchell, D. L., Chai, S. K., Liu, Y., Heymsfield, A. J., and Dong, Y.: Modeling cirrus clouds. Part I: Treatment of bimodal size spectra and case study analysis, Journal of the atmospheric sciences, 53, 2952–2966, https://doi.org/https://doi.org/10.1175/1520-0469(1996)053<2952:MCCPIT>2.0.CO;2, 1996.

Morrison, H., van Lier-Walqui, M., Fridlind, A. M., Grabowski, W. W., Harrington, J. Y., Hoose, C., Korolev, A., Kumjian, M. R., Milbrandt, J. A., Pawlowska, H., Posselt, D. J., Prat, O. P., Reimel, K. J., Shima, S.-I., van Diedenhoven, B., and Xue, L.: Confronting the Challenge of Modeling Cloud and Precipitation Microphysics, Journal of Advances in Modeling Earth Systems, 12, https://doi.org/10.1029/2019MS001689, 2020.

Morrison, H., Milbrandt, J. A., and Cholette, M.: A complete three-moment representation of ice in the Predicted Particle Properties (P3) microphysics scheme, Journal of Advances in Modeling Earth Systems, 17, e2024MS004 644, https://doi.org/10.1029/2024MS004644, 2025.

Ori, D., von Terzi, L., Karrer, M., and Kneifel, K.: snowScatt 1.0: Consistent model of microphysical and scattering properties of rimed and unrimed snowflakes based on the self-similar Rayleigh-Gans approximation, Geoscientific Model Development, 14, 1511–1531, https://doi.org/10.5194/gmd-14-1511-2021, 2021.

https://doi.org/10.5194/egusphere-2025-3910
Preprint. Discussion started: 9 September 2025

Oue, M., Tatarevic, A., Kollias, P., Wang, D., Yu, K., and Vogelmann, A. M.: The Cloud-resolving model Radar SIMulator (CR-SIM) Version 3.3: description and applications of a virtual observatory, Geoscientific Model Development, 13, 1975–1998, https://doi.org/10.5194/gmd-13-1975-2020, 2020.

Petty, G. W. and Huang, W.: Microwave backscatter and extinction by soft ice spheres and complex snow aggregates, Journal of the Atmospheric Sciences, 67, 769–787, https://doi.org/10.1175/2009JAS3146.1, 2010.

Pruppacher, H. R. and Klett, J. D.: Microphysics of Clouds and Precipitation, Kluwer Academic Publishers, Dordrecht, https://doi.org/10.1007/978-0-306-48100-0, 1997.

Reiter, C. A.: A local cellular model for snow crystal growth, Chaos, Solitons & Fractals, 23, 1111–1119, https://doi.org/10.1016/j.chaos.2004.06.071, 2005.

Roweis, S., Hinton, G., and Salakhutdinov, R.: Neighbourhood component analysis, Adv. Neural Inf. Process. Syst.(NIPS), 17, 4, https://web.archive.org/web/20230607061223/https://proceedings.neurips.cc/paper_files/paper/2004/file/42fe880812925e520249e808937738d2-Paper.pdf, 2004.

Schrom, R. S. and Kumjian, M. R.: Bulk-density representations of branched planar ice crystals: Errors in the polarimetric radar variables, Journal of Applied Meteorology and Climatology, 57, 333–346, 2018.

Schrom, R. S. and Kumjian, M. R.: A probabilistic radar forward model for branched planar ice crystals, Journal of Applied Meteorology and Climatology, 58, 1245–1265, https://doi.org/10.1175/JAMC-D-18-0204.1, 2019.

Sorensen, C. M.: Light scattering by fractal aggregates: a review, Aerosol Science & Technology, 35, 648–687, https://doi.org/10.1080/02786820117868, 2001.

Takahashi, T.: Influence of Liquid Water Content and Temperature on the Form and Growth of Branched Planar Snow Crystals in a Cloud, Journal of the Atmospheric Sciences, 71, 4127–4142, https://doi.org/10.1175/JAS-D-14-0043.1, 2014.

von Terzi, L.: Codes used to generate the data and figures for this paper, https://doi.org/10.5281/zenodo.17079588, 2025a.

von Terzi, L.: McRadar, https://doi.org/10.5281/zenodo.17079541, 2025b.

von Terzi, L., Dias Neto, J., Ori, D., Myagkov, A., and Kneifel, S.: Ice microphysical processes in the dendritic growth layer: a statistical analysis combining multi-frequency and polarimetric Doppler cloud radar observations, Atmospheric Chemistry and Physics, 22, 11 795–11 821, https://doi.org/10.5194/acp-22-11795-2022, 2022.

von Terzi, L., Ori, D., and Kneifel, S.: level1-data, https://doi.org/10.5281/zenodo.16792943, 2025.

Welss, J.-N., Siewert, C., and Seifert, A.: Explicit habit-prediction in the Lagrangian super-particle ice microphysics model McSnow, Journal of Advances in Modeling Earth Systems, 16, e2023MS003 805, https://doi.org/10.1029/2023MS003805, 2024.

Westbrook, C. D., Ball, R., Field, P., and Heymsfield, A. J.: Universality in snowflake aggregation, Geophysical research letters, 31, https://doi.org/10.1029/2004GL020363, 2004.

Yurkin, M. A. and Hoekstra, A. G.: The discrete dipole approximation: an overview and recent developments, Journal of Quantitative Spectroscopy and Radiative Transfer, 106, 558–589, https://doi.org/10.1016/j.jqsrt.2007.01.034, 2007.

Yurkin, M. A. and Hoekstra, A. G.: The discrete-dipole-approximation code ADDA: capabilities and known limitations, Journal of Quantitative Spectroscopy and Radiative Transfer, 112, 2234–2247, https://doi.org/10.1016/j.jqsrt.2011.01.031, 2011.